UC Santa Barbara
UC Santa Barbara Electronic Theses and Dissertations

Title

The Effect of Grain Size on Deformation Twinning in Magnesium

Permalink

https://escholarship.org/uc/item/3v835174

Author

Buzolits, Anna Elizabeth

Publication Date

2019

Peer reviewed|Thesis/dissertation

UNIVERSITY OF CALIFORNIA

Santa Barbara

The Effect of Grain Size on Deformation Twinning in Magnesium

A Thesis submitted in partial satisfaction of the requirements for the Masters of Science in

Mechanical Engineering

by

Anna Elizabeth Buzolits

Committee in charge:

Professor Samantha Daly, Chair

Professor Irene Beyerlein

Professor Jeff Moehlis

December 2019

The thesis of Anna Elizabeth Buzolits is approved.

_____

Irene Beyerlein

_____

Jeff Moehlis

_____

Samantha Daly, Committee Chair

September 2019

ACKNOWLEDGEMENTS

ABSTRACT

The Effect of Grain Size on Deformation Twinning in Magnesium

by

Anna Elizabeth Buzolits

There is great interest in magnesium and magnesium alloys for use as structural materials due to their high strength-to-weight ratio compared to aluminum and steel. However, the relationship between the macroscopic failure behavior of magnesium and the micro- and mesoscopic deformation mechanisms in magnesium are relatively poorly understood. Basal slip is ubiquitous in magnesium deformation, but the factors that determine the secondary deformation mechanisms, non-basal slip and twinning, are less well studied. For this reason, the aim of this study was to identify the relationship between twin occurrence and grain size. Towards this goal, a combination of electron backscatter diffraction (EBSD), scanning electron microscope digital image correlation (SEM-DIC) were used to capture full-field strain maps of a ~1mm x 1mm field of view on a pure magnesium dogbone sample under monotonic compression. It was found that the likelihood that a grain exhibits twinning increases as the size of the grain increases. K-means clustering, filtered cross-correlation, and an AlexNet convolutional neural network (CNN) were also used to attempt to automate the twin identification process. Though the results of this work exhibited the same trend (increased twin likelihood with increased grain size), the precision, sensitivity, and accuracy of these methods was analyzed and it was found that more work needs to be done before significant conclusions can be drawn from their results.

1. Introduction

Over the past several decades, computational materials research has been greatly accelerated by advancements in available computing power. Computational and theoretical materials research, particularly predictive modeling, has in turn contributed to improved development processes for new materials. However, the potential of these methods is not being fully exploited, due to the limited ability theoretical research groups have to share and collaborate with each other and with experimentalists who can help inform their models.

The Materials Genome Initiative (MGI) was established in 2011 with the goal of improving collaboration between theorists and experimentalists, towards accelerating new material development while simultaneously reducing the associated costs. Integrated Computational Materials Engineering (ICME), one major aspect of the MGI, was founded with the idea that acceleration and cost reduction can be more effectively addressed through theoretical and experimental collaborations. Theoretical models, which aim to predict material behavior, are informed by the results of experimental work, which can quantitatively validate the results of a model and also reveal qualitative information about the mechanical behavior and microstructural impact on deformation in an actual material. Therefore, an iterative loop is created wherein empirical data informs models, which in turn are validated by experiment. This entire process requires the ability for research groups in different departments or at different institutions to collaborate closely.

The PRedictive Integrated Structural Materials Science (PRISMS) center is a collaborative effort between the University of Michigan and the University of California, Santa Barbara, which aims to improve the materials research community's ability to collaborate and accelerate the materials

design process. The PRISMS center has three main aspects: PRISMS codes, the Materials Commons, and Integrated Collaborative Science.

The PRISMS codes are a library of open-source models, available on GitHub, which have been/are being developed by members of the PRISMS center. These codes include CASM (statistical mechanics), DFT-FE (Real-space DFT calculations using Finite-elements), PRISMS-PF (Phase Field), PRISMS-Plasticity, and PRISMS Integration Tools. According to the center's documentation *"The PRISMS integrated computational codes for multiscale materials modeling allow for fast development of large-scale numerical frameworks for various mathematical models of material behavior (Continuum Plasticity, Crystal Plasticity, Phase Field, Statistical Mechanics, DFT, etc)."* [36] The Materials Commons is an online repository and collaboration platform for researchers from different institutions to organize, publish, and share their models, experimental data, and methods. This site fosters the bridge between materials computation and experimentation, a key component in the acceleration of material design. It also allows researchers to track the process of their work and can be integrated with many other tool sets. Integrated Collaborative Science is the term used for the work done by PRISMS' "use case" groups, which are examples of how PRISMS methods can be applied to the research and collaboration of different research groups. These use case groups "*link experiments with the simulations, validate the models, and improve the codes.*" [36]

The main goal of this work was to identify the relationship between twin nucleation and grain size in pure magnesium, therefore improving the understanding of the link between deformation mechanisms and microstructure**.** Magnesium and magnesium alloys were chosen as the proof-of-concept materials to validate the PRISMS protocols, due to their high potential for use as structural materials combined with the current gaps in knowledge towards predicting magnesium behavior,

even with several high-quality studies that have been conducted, due to the complexity of its mechanical response. The work described in this thesis was performed as a "use case" with the aim of helping to validate the models developed by computationalists at the University of Michigan.

2. Literature Review

Magnesium alloys are great candidates for lightweighting, due to their high strength-to-weight ratios, as compared to currently-used materials such as steel and aluminum. Passenger vehicles are major contributors to the increasing concentration of greenhouse gases in our atmosphere. To decrease the greenhouse gases produced by automotive vehicles, their fuel efficiency must be improved; one significant way to do this is by making them lighter. It has been estimated that lightweighting with magnesium could lead to a weight reduction of between 30 and 70% for a passenger car. [32] If this were applied to a quarter of the vehicles in the United States, this would result in an annual savings of over five billion gallons of fuel. [32]

There is considerable excitement surrounding the potential of magnesium for lightweighting, but its use is hampered in a practical sense by the low formability of currently available magnesium alloys. It is known that formability can be significantly impacted by the addition of alloying elements (such as rare earth elements) and processing routes. However, a trial-by-error approach towards understanding the material and processing design spaces is not tractable. To make meaningful gains in improving magnesium's properties, there must be a fundamental understanding of the complex, interconnected relationships between processing and the observed macroscopic behavior of these alloys.

2.1 Processing Effects

Wrought magnesium has failed to gain widespread application, in part due to its low ductility. The relative brittleness of magnesium/alloys leads to poor room temperature formability, meaning that "hot" processing methods are required to produce usable magnesium goods. However, these methods, i.e. extrusion or rolling, cause the material to exhibit a strong basal texture. This occurs due to the grain rotation that accompanies the simple shear strain felt by the grain. When grains within polycrystals experience this rotation, they tend to orient themselves in accordance with the applied deformation and the symmetry of the deformation modes. [2]

In magnesium (and other HCP metals with c/a ratios of less than 3), this means that the grains in the polycrystal are all similarly oriented such that the c-axis is perpendicular to the process direction. This comes from the fact that, in magnesium, favorably-oriented grains (those with c-axes perpendicular to the compression axis) display $<10\bar{1}2>$ tension twins, which rotate the crystals such that the c-axis is almost parallel to the axis of applied compression. Therefore, the texture created by extrusion and rolling (which compress the material while it moves through the respective apparatus), are such that the c-axis for most grains lies perpendicular to the extrusion/rolling-direction. The strength of this basal texture can vary from alloy to alloy, and it affects the deformation modes active in the alloy. [2]

2.2 Deformation Mechanisms in Magnesium Alloys

Magnesium alloys have a hexagonal close packed (HCP) crystal structure with four independent slip systems: basal slip $0001<11\bar{2}0>$, prismatic slip $\{10\bar{1}0\}<11\bar{2}0>$, pyramidal <a> slip $\{10\bar{1}1\}<11\bar{2}0>$, and pyramidal <c+a> slip $\{11\bar{2}2\}<11\bar{2}3>$. They also exhibit 2 twinning modes: $\{10\bar{1}2\}<10\bar{1}1>$ twinning or tension twinning accommodates c-axis tensile strain, and

$\{10\overline{1}1\}<10\overline{1}2>$ twinning or compression twinning accommodates c-axis compressive strain. These two twinning modes are required for compliance with the von Mises criterion, which requires five independent deformation mechanisms in a polycrystalline material to accommodate arbitrary deformation.
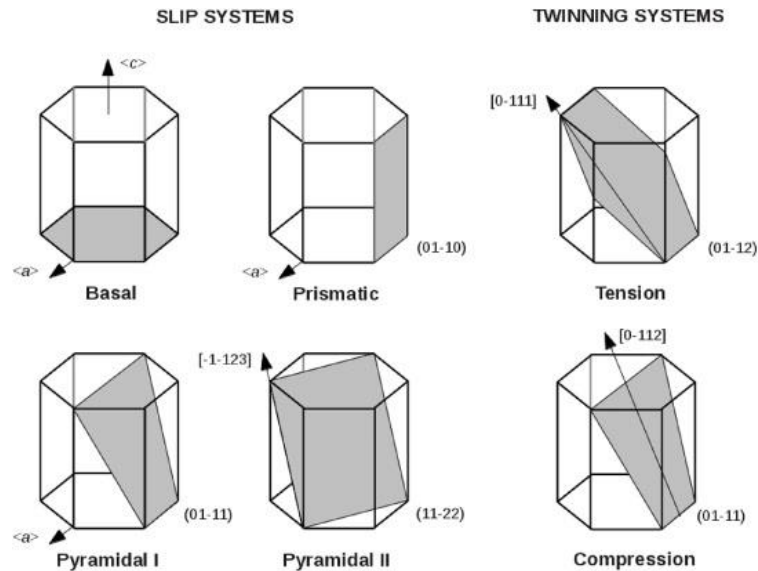
Figure 1. Possible slip and twinning systems in a hexagonal close-packed crystal. (Image from [32])

Basal slip, which is slip along the close-packed plane, is the most easily activated deformation mechanism in magnesium and its alloys. This preference for basal slip is increased by the strong basal texture which most magnesium/alloys exhibit. The critical resolved shear stresses (CRSS) of the other deformation mechanisms (non-basal slip and twinning) are affected by many variables, such as alloying elements, the direction of the applied strain, the ambient temperature, and microstructural factors including for example grain size and precipitate content. Given the complexity of these interrelated factors and their effects, there is much discussion in the community about what the actual CRSS values are. In general, it is accepted that, for

polycrystalline magnesium at room temperature under quasi-static loading, $CRSS_{basal} < CRSS_{tensile\text{-}twinning} < CRSS_{prismatic} < CRSS_{pyramidal}$.

The macroscopic stress-strain curves for magnesium alloys change significantly depending on the relative activity of non-basal slip and twinning. When non-basal slip is the dominant secondary deformation system (after basal slip), a concave-down curve is produced. However, when twinning is the dominant secondary system, the alloys exhibit a great deal of strain hardening due to the role of twin boundaries as barriers to slip. This leads to a concave-up portion of the stress/strain curve. [4] This trend enables identification of the dominant secondary deformation system in different testing and microstructural conditions and has led to the identification of several relationships between test parameters, microstructure, and deformation mechanisms in magnesium alloys.
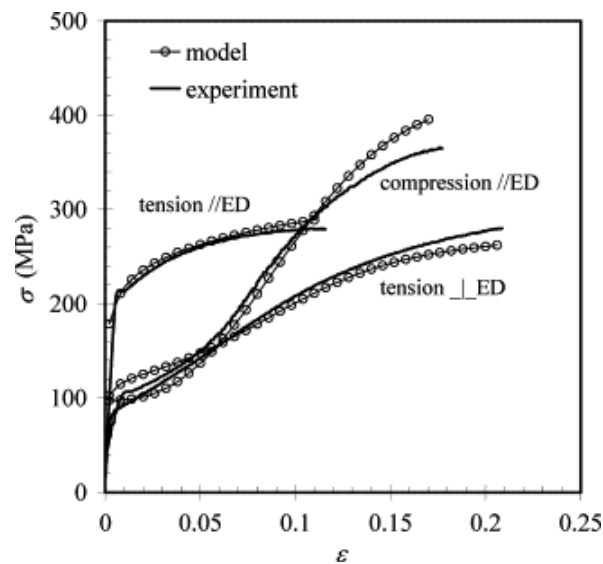
Figure 2. "True stress-strain curves obtained from commercial extruded AZ31 bar. Twin-dominated plasticity is evident in the strain hardening exhibited by the "compression//ED" curve and the "tension _|_ ED" curve. The "tension//ED" curve exhibits slip-dominated plastic behavior." (Figure 8 from [4])

Studies have shown that, at room and slightly elevated temperatures, twinning is activated before non-basal slip when a magnesium alloy sample is tested parallel to the extrusion direction in compression [2] or perpendicular to the extrusion direction in tension. [4] Both of these global strain states lead to c-axis tension, due to the aforementioned texture exhibited by magnesium alloys. The relatively low CRSS for tensile twins compared to non-basal slip modes means that, when crystals are oriented in this preferential way, tensile twins will activate to accommodate c-axis strain before <c+a> slip modes.

Magnesium and its alloys with higher average grain sizes exhibit a greater amount of twinning than those with lower average grain sizes. Additionally, the larger grains in the microstructure have also been shown to undergo larger twinned volumes than smaller grains. [6] [10] The reasons for the effects of grain size on twinning are not well understood, but there are theories on why these trends exists.

The largest barrier for twins to occur is stress required to nucleate a twin. By comparison, twin growth requires much lower stresses. [34] Twins most commonly nucleate due to stress concentrations at grain boundaries. It follows, then, that increased grain boundary area (which increases with grain size) will affect the propensity for twin nucleation. According to a study by Wang et. Al in 2010 [49], the local stress state at a grain boundary, the characteristics of the grain boundary dislocations, and the grain boundary surface area all affect the number of nucleation events that occur at a grain boundary. Using a Poisson probability distribution, Eq. 1 shows the

likelihood that the number of stable twin nuclei (N) formed in a grain boundary surface area a* is equal to κ:

$$P(N = \kappa, a^*) = \frac{(\lambda a^*)^\kappa}{\kappa!} \exp(-\lambda a^*)$$

Equation 1.

where λ is the process rate and has units of density per unit area of a^*.

$$\lambda(\tau) = \frac{1}{a_0}\left(\frac{\tau}{\tau_0}\right)^\alpha$$

Equation 2.

where a_0 is "a characteristic area (or length scale) in which only one twin is expected," τ is the local stress, α is a material property associated with dispersion in the nucleation process, and τ_0 is the threshold stress for activating a grain boundary dislocation. [49] From this, the probability that at least one stable twin embryo will be formed from a^* can be found using Eq. 3:

$$P(N \geq 1, a^*) = 1 - P(N = 0, a^*) = 1 - exp\left[-\frac{a^*}{a_0}\left(\frac{\tau}{\tau_0}\right)^\alpha\right]$$

Equation 3.

Furthermore, the average number of twin nuclei formed in a^* can be found using Eq. 4:

$$\langle N(a^*)\rangle = \frac{a^*}{a_0}\left(\frac{\tau}{\tau_0}\right)^\alpha$$

Equation 4.

As shown by Eq. 4, the average number of stable twin nuclei produced by a grain boundary increases as the grain boundary surface area, a^*, increases. [49]

Commonly, the stress to nucleate a twin is produced by dislocation pile-ups in neighboring grains. The stress caused by these pile-ups is proportional to the distance they have traveled from their source (somewhere within the grain) to the grain boundary between the two neighboring grains. In larger grains, the average distance from any source to any grain boundary is large compared to small grains, and therefore the stresses caused by the pile-ups can be large enough to nucleate twins. This indicates that samples with larger average grain sizes will exhibit more twins, because a grain's neighbor is more likely to be large and exhibit large pile-up stresses. In contrast, non-basal slip in Mg is often caused by stress concentrations due to the compatibility stresses, which keep grain boundaries from fracturing. These stresses have been shown to penetrate ~10μm into a grain, regardless of grain size. This means that in grains larger than ~20μm, there are areas in which non-basal slip will not occur due to compatibility stresses. [34]. However, the fraction of twinned grains in samples of different average grain sizes has been shown not to be dependent on that average grain size. [10]

These interactions are not fully characterized or understood, in part due to the difficulties inherent in the experimental characterization of magnesium and its alloys. Magnesium is highly susceptible to oxidation and corrosion, which precludes many experimental approaches, and much of the information on their microstructure-property interactions comes from tests that produce low volumes of data. To make statistically sound conclusions on these interconnected relationships, there is a critical need for high-resolution, large field-of-view data describing the interactions between microstructure and deformation across length scales.

2.3 Scanning Electron Microscopy Digital Image Correlation (SEM-DIC)

Digital Image Correlation (DIC) is a non-contact, length-scale-independent experimental method which tracks changes in a (speckle) pattern on a sample's surface in a sequence of images to produce full-field deformation maps. DIC is a length scale independent calculation, where the quality of the pattern and the minimization of image distortion are important to the quality of the resulting calculation. DIC can be applied to scanning electron microscopy (SEM) images to produce full-field, nanometer spatial resolution strain maps of an area of interest (AOI). At the most basic level, this is done by a three step process: 1. Apply a speckle pattern to the surface of the sample, 2. Image the AOI before (for reference) and after deformation, using a SEM, and 3. Use computer software to analyze the images and calculate the surface displacements and strains by comparing the "reference image" to the "deformed image." DIC has been used extensively as a tool to study the mechanics of materials since the 1980s. It almost exclusively utilized optical methods until the SEM-DIC method was pioneered in the mid-2000s. [23] [44-46] SEM-DIC can be used to evaluate dislocation slip [19], void formation [41], fracture and fatigue behavior [12] [21] [48], grain boundary sliding, and cracking during creep [11].
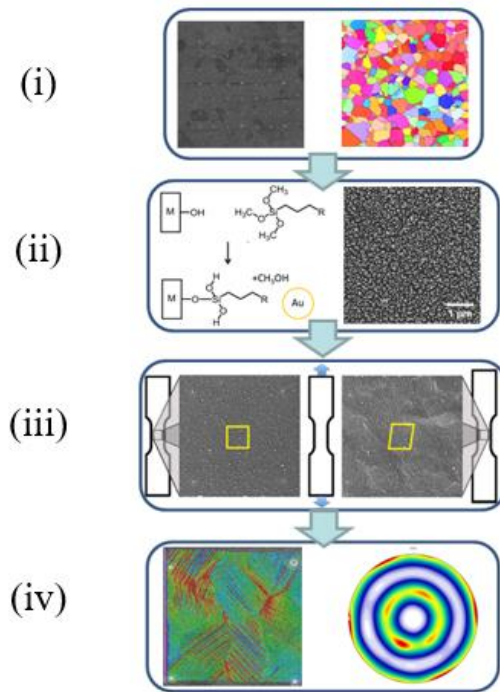
Figure 3. Schematic showing the steps involved in SEM-DIC including (i) AOI selection and EBSD, (ii) patterning, (iii) imaging at several strain levels, and (iv) image correlation and comparison with EBSD data. (Image courtesy of Z. Chen).

Before the SEM-DIC process began, the AOI was identified using an SEM and marked using electron beam platinum deposition, and Electron Backscatter Diffraction (EBSD) was performed. Following EBSD, a speckle pattern was applied to the surface of the sample.

2.3.1 Patterning

In order to achieve the ideal speckle pattern, several guidelines should be followed [30]:

1. The speckle pattern must cover the entire AOI.

2. The speckles must be uniform in size but randomly distributed over the AOI.

3. The speckles are strongly bonded to the surface of the sample but be much more easily deformable than the sample OR be strongly bonded to the surface and move with the deformation of the sample. [8]

4. Images should be taken, and speckles sized, such that each speckle is made of no less than 3x3 pixels and no more than 7x7 pixels. The lower limit is to prevent aliasing, strains/displacements which are falsely reported due to smoothing effects from low resolution. [38] The upper limit is to ensure the presence of enough DIC data points. [40]

5. The pattern must exhibit a broad bimodal grayscale histogram, indicating a good mix of bright and dark areas in the AOI, to reduce error. [46] The edges of the speckles making up the pattern should not be sharp, but rather fade in with the background, as to prevent aliasing. [39]

6. The pattern (speckle shape, density, etc…) should not be affected by the testing environment (changing temperatures, pressures, etc…)

7. The speckle pattern should represent about 50% of the AOI. Pattern densities much higher or lower than 50% result in incorrect strain feature identification. [40]

There are many potential material and application options for DIC patterns, including paints, dyes, inks, powders, and lithographs. The method applied herein uses gold nanoparticles and was adapted by A.D. Kammers and S. Daly [24] in 2013. This method has been shown to be highly effective for SEM-DIC on a variety of metal, ceramic, and polymer materials. The pattern is created by first functionalizing the sample's surface by submerging it in a solution of water and (3-Aminopropyl)triethoxysilane (APTMS). Once the silane is attached to the sample surface, the sample is submerged in gold nanoparticles, which have been synthesized by the Frens method. The specific details of how the sample in this test was patterned can be found in Section 3.

2.3.2 Imaging

A fundamental problem within the mechanics/materials community is the capture and processing of data sets large enough to be statistically significant representations of the microstructural variations in large material surfaces or volumes. Therefore, with the goal of capturing high-resolution, microscale displacement fields over relatively large (mm-scale) fields of view, a multi-tile imaging approach was adopted for this test, wherein full-field displacements, strains and microstructure are captured for each image tile. This was done using external scan control, a method for automating image capture in an SEM introduced by Lenthe et al. [29]

The size and resolution of the captured images was chosen such that each speckle was imaged by between 3x3 pixels and 7x7 pixels (per rule 4 in section 2.3.1). For the purpose of stitching images together during data analysis, an at least 20% overlap between adjacent images (both horizontally and vertically) is used. In this test, the AOI was 1mm x 1mm, and each image tile was 82μm x 82μm with a resolution of 4096 x 4096 pixels. The corner images were centered on the corners of the AOI, so in total the images covered 1.082mm x 1.082mm. 22 rows of 22 images were taken to cover this entire area.
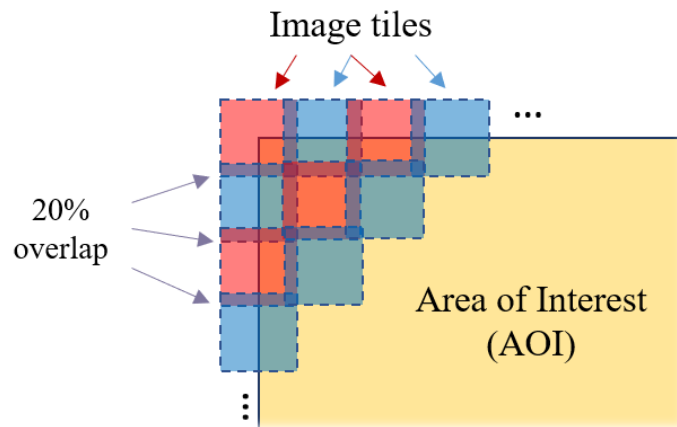
Figure 4. Diagram representing how each tile image was
taken, with 20% overlap on each side, to make up the full
area of interest.

The positions of the image tiles were determined using a bilinear interpolation. With a grid of R x

C images an image's position is determined as a function of its row, r[0,R], and the column, c[0,C]:

P(r, c) = (x, y). The positions of the images at each corner of the grid, P(0, 0), P(0, C), P(R, 0), and

P(R, C), are determined by the user before each set of images is captured using the previously

applied markers. For the images in the 0th and R^{th} rows and in an arbitrary "c^{th}" column, the

following linear interpolation was applied:

$$P(0,c) = \frac{C-c}{C} P(0,0) + \frac{c}{C} P(0,C) \hspace{3cm} \text{Equation 5}$$

$$P(R,c) = \frac{C-c}{C} P(R,0) + \frac{c}{C} P(R,C) \hspace{3cm} \text{Equation 6}$$

For the image in the cth column and arbitrary "r^{th}" row:

$$P(r,c) = \frac{R-r}{R} P(0,c) + \frac{r}{R} P(R,c) \hspace{3cm} \text{Equation 7}$$

Substituting in the expressions for P(0,c) and P(R,c) into the expression for P(r,c) results in:

$$P(r,c) = \frac{1}{R*C}((R-r)*(C-c)*P(0,0) + (R-r)*c*P(0,C) + r*(C-c)*P(R,0) + r*c*P(R,C))$$

$$\text{Equation 8}$$

This relationship was used to determine the position of an image in an arbitrary row and column.

To capture each image, the electron beam is directed to each pixel and held for the assigned dwell time. The pixel is sampled multiple times and the sampled detector data is stored in an array for each pixel and image stacks are created from the elements in the same position for each pixel's array. For example, the Nth image in the stack is made up of the data from the Nth element in each array. For this experiment, the beam was sent in a raster pattern (rather than snake; see Figure 5) with the addition of a wait time equal to 16% of the time taken to scan the entire line. This was because the required dwell time to obtain reference images with minimal distortion is far shorter than the dwell required for snake scanning.
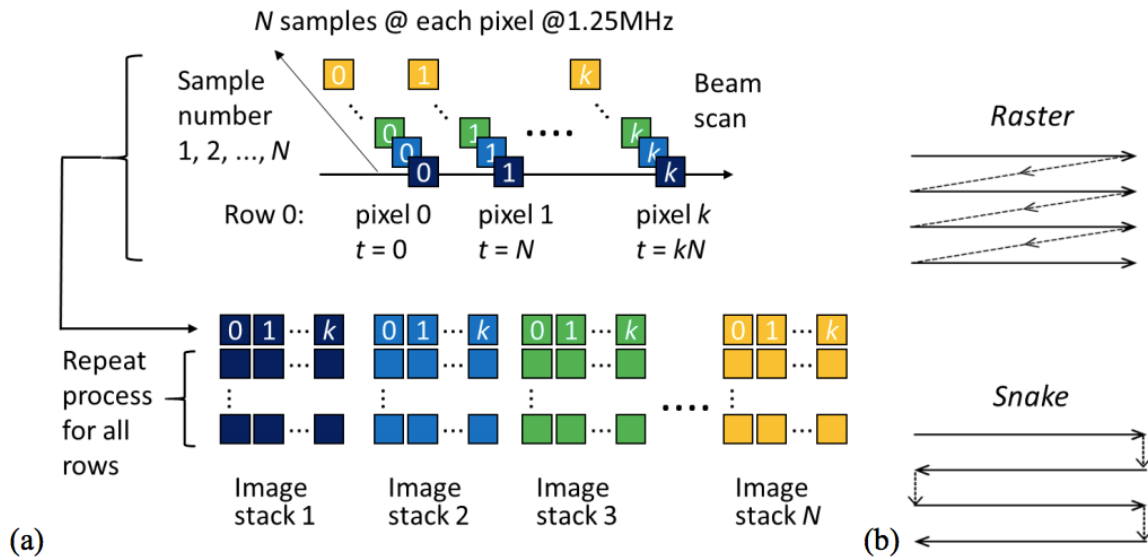
Figure 5. "Illustration of the imaging algorithm with the custom external scan controller. (a) The electron beam was driven by the scan signal to sequentially reach each of the target pixel positions. At each pixel position, the detector signal was sampled multiple times (with the data indicated by the colored squares) and stored in an array. The N-th sample in the array of each pixel was used to construct the N-th image stack. (b) Illustration of the electron beam path in the raster scan mode and snake scan mode." (Figure 4 from [16])

Spatial and temporal drift distortions occur inside the SEM which can greatly reduce the accuracy of the strain data calculated by SEM-DIC, and corrections have been developed in order to mitigate these distortions. [44] [45] However, the external scan control developed by Lenthe et al [29] and utilized in this work reduced these distortions to the extent that drift and spatial distortion corrections were no longer required.

Figures 6 and 7 [16] show examples of spatial distortions which have been observed at different length scales and in at least two different microscopes: a FEI Teneo SEM and a Tescan Mira 3 SEM. The external scan control method utilized in this work has been shown to greatly reduce spatial distortions of this type.

Figure 6 shows cross-hatched (Figure 6(b)) and vertical/diagonal (Figure 6(c)) spatial distortion noise patterns produced when the stock scan controller was used to image a sample subjected to a

rigid body translation. Figure 6(d) shows that this distortion is all but mitigated when external scan control is applied.
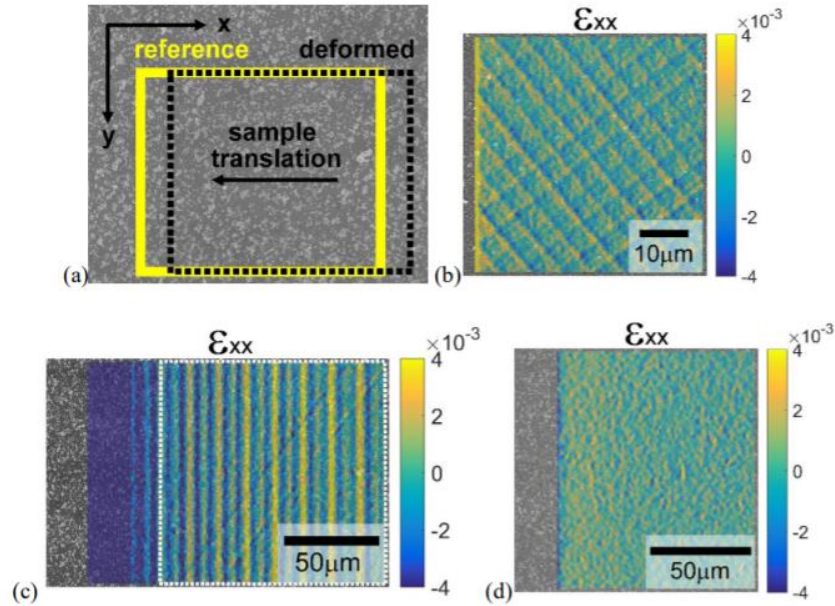
Figure 6. Spatial distortion patterns vary depending on several variables including the microscope used to capture the images, and these distortions can be mitigated by using external scan control. (a) An illustration of the rigid body displacement undergone by the sample. (b) Cross-hatched noise patterns appear in the DIC strain map when a sample was translated 2μm and imaged using the stock controller in a Tescan Mira 3 SEM. (c) The vertical and diagonal distortion patterns were a result of imaging a sample having undergone a translation of 20μm in a FEI Teneo SEM with stock scan control. (d) External scan control, applied to image a 20μm translation in a FEI Teneo SEM, resulted in minimal spatial distortion. Note: (c) and (d) were produced from the same area of the same sample in the same microscope. The same pixel resolution was used and the image parameters were adjusted so that the image time was approximately 45 seconds for each image. The imaged area in (d) is represented by a white box on (c). (Figure 2 from [16])

A different form of spatial distortion, wherein the relative position of the same features were not the same in different images is shown in Figure 7. [16] In this study, the sample was subjected to a rigid body translation close to the width of the FOV. The resulting images show that features were imaged differently depending on their location in the image and that the distortion is worse

close to the left side of the image. This left-side distortion prevents the high-quality overlay necessary for stitching neighboring images and thus the entire AOI. Therefore, the size and number of recorded image tiles was chosen such that there was an approximately 20% overlap between tiles. This allows for capturing overlapping images and deleting the distorted data to ensure the spatially distorted data does not get included in the final displacement and strain maps. The external scan control imaging method used for this experiment has been shown to greatly decrease this spatial distortion (see Figure 7. 3(c)), so the overlap area served a different purpose (identifying image location for stitching, see section 3.4.2).
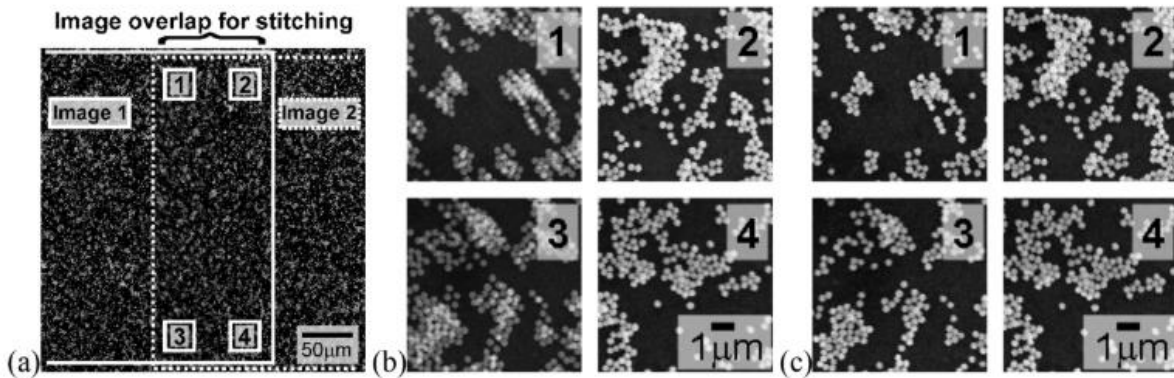
Figure 7. Image stitching is greatly affected by the spatial distortions present in the overlay between two FOVs, and these distortions can be mitigated using external scan control. (a) Two images with a stitching overlap region in the center and four small areas labeled 1-4 to be magnified for observation in (b) and (c). (b) The magnified areas of the overlap region, captured with the internal/stock scan control, show that the image quality can vary greatly depending on location. (c) When imaged using external scan control, the same regions are imaged with more consistent quality and minimal spatial distortion. (Figure 3 from [16])

3. Material and Methodology

3.1 Sample Preparation

3.1.1 Polishing

Dogbone-shaped samples of pure magnesium were cut using electrical discharge machining (EDM). The dimensions of the manufactured samples are shown Figure 8. Samples were prepared for testing using the techniques developed in [20]. Specimens were mechanically polished as follows: dogbone-shaped test specimens were mounted onto the head of a Buehler autopolisher using crystalbond, with the head and base speeds set to 60rpm and 120rpm respectively and the force set to 20N. The samples were metallographically ground with 600 (2 minutes), 800 (4 minutes), 1200 (5 minutes), and P4000 (until sample surface was uniformly textured, as seen under an optical microscope, about 6 minutes) standard ANSI grit silicon carbide paper. Each individual paper was only used for 30 seconds. Next, the samples were polished with 3μm and 1μm water-based diamond suspensions (MetaDi Ultra Paste) for 10 and 15 minutes, respectively. The polishing pad was first lubricated with MetaDi Fluid and then ~5 dots of the diamond paste were distributed around the pad. Following each diamond polishing step, each sample was rinsed with Simple Green soap, deionized (DI) water, and NaOH, then dried with compressed air for ~10 seconds. Finally, a 2:1 ratio of water to a high pH colloidal alumina/colloidal silica mixture from Buehler (MasterPolish) was used to chemo-mechanically polish each sample for 15 minutes, after which each sample was rinsed with soap, water, and NaOH, then dried with compressed air for ~10 seconds. This MasterPolish step was performed by first lubricating the polishing pad with MetaDi Fluid and using a 3ml disposable pipette to place ~10 dots of the MasterPolish/Water solution, distributed evenly over the pad. More MasterPolish/Water solution was added to the polishing pad, using a pipette, at a rate of about 1 drop every 2 seconds. To remove the sample

from the polishing head, a razor blade was slid under the sample to break the crystalbond. Acetone

and a q-tip were used to remove excess adhesive from the back side of the sample.
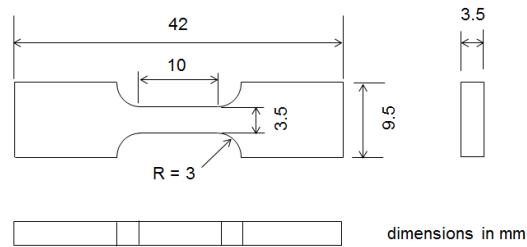
Figure 8. Magnesium dog bone samples were Electrical Discharge Machined to these specifications. (From Figure 1 from [16])

3.1.2 Etching, Platinum Deposition, & EBSD

Following mechanical and chemical polishing, the samples, which were handled with plastic

forceps, were etched in a solution of 50 ml methanol + 6 ml hydrochloric acid + 4 ml nitric acid

for five seconds before being rinsed in DI water (10 seconds) and ethanol (10 seconds), then dried

with compressed air until no liquid remained on the sample. Immediately following this etching

process, the sample was mounted on a Scanning Electron Microscope (SEM) Pin Stub Specimen

Mount and placed inside an FEI Teneo SEM. Markers were placed in the corners of the area of

interest (AOI), an area near the center of the gauge section which was mostly free from debris or

imperfections, using Pt deposition. This was done to make locating the AOI easier in the future.

For the Pt deposition process, the microscope's voltage was set to 2kV while the beam current was

0.4nA. The stage was set to the eucentric point, about 14μm, by finding the working distance at

which the beam does not change location regardless of to what angle the stage is tilted. Rectangles

of dimensions 5x15μm were placed at three of the corners of the AOI while at the fourth corner a

15x5μm rectangle was deposited, as to make clear the orientation of the AOI. Each rectangle was deposited 10nm tall.

An Electron Back-Scatter Diffraction (EBSD) map was taken of the AOI on the samples using TSL OIM software on the FEI Teneo SEM. The accelerating voltage was 20kV, the working distance was 14mm, the spot size was 6 and the EBSD step size was 1μm.
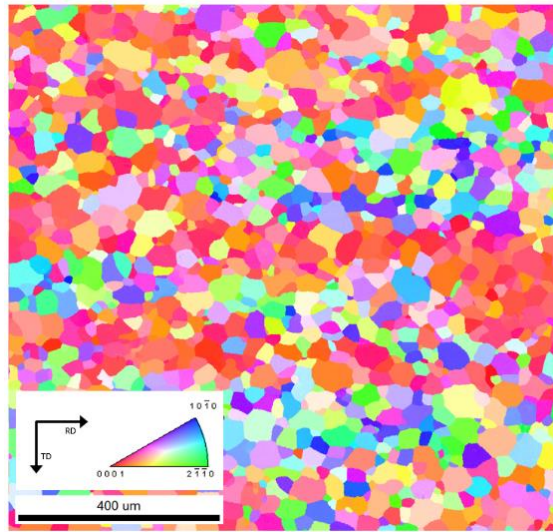
Figure 9. The EBSD map of the full AOI, collected using the TSL OIM software on a FEI Teneo SEM.

3.1.3 SEM-DIC Patterning

Next, a speckle pattern was applied to the surface of the test specimen for microscale deformation tracking by Scanning Electron Microscope Digital Image Correlation (SEM-DIC). Gold (Au) nanoparticles were fabricated using the Frens method and the pH of the nanoparticle solution was subsequently adjusted using NaOH in order to prevent corrosion of the sample, per [20]. Samples

were submerged in a solution of 5% APTMS, 50% DI water, and 45% Ethanol for 15 minutes, then rinsed with DI water, ethanol, and dried with compressed air until no liquid remained on the sample. They were then submerged in vials of Au nanoparticles with the specimen face of interest facing down. Samples were left in the nanoparticle solution until the nanoparticles degraded (changed color, usually becoming a dark grey, and/or the particles and the water separated, creating a gradient in color), whichever came first. Once degradation of the nanoparticle solution occurred by one of these two mechanisms, the sample was removed from the solution. The pattern on the sample was inspected in the SEM and it was determined that the pattern was not dense enough for testing. Therefore, the sample was placed in a new vial of nanoparticle solution and the process was repeated.
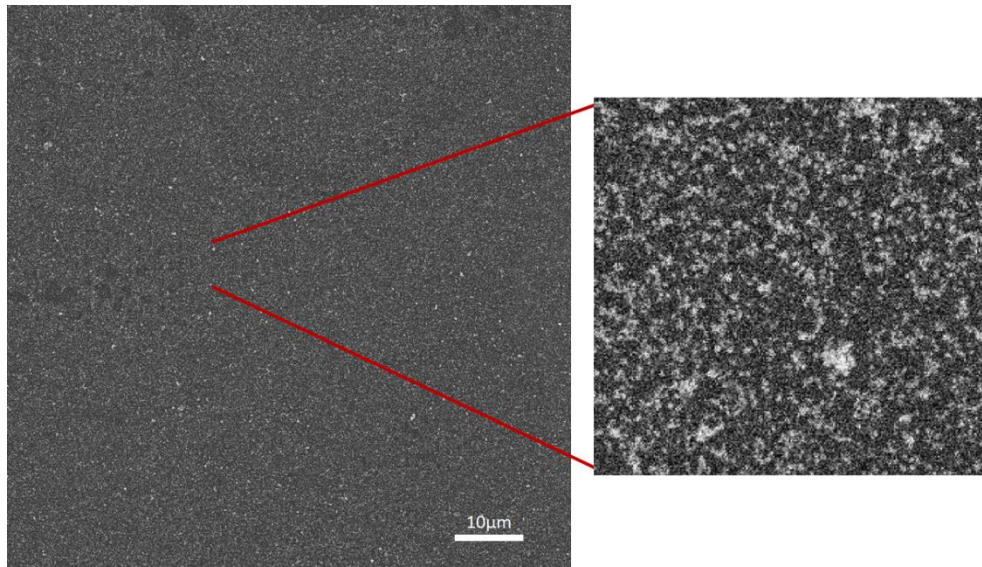
Figure 10. The final speckle pattern was produced using the Frens method, altered by 1) neutralizing the nanoparticle solution by adding NaOH until the pH was 12 and 2) repeating the step during which the sample was submerged in the nanoparticle solution.

3.2 Imaging with External Scan Control

3.2.1 Microscope Setup

Once the pattern was acceptably dense (Figure 10), the SEM was configured to use the External Scan Control to take the images required for SEM-DIC [29]. First, a Kyowa brand general purpose foil strain gauge (strain limit = 5%) was applied to the back side of the sample using Kyowa brand strain gauge glue. The sample was then secured into the custom Kammrath and Weiss loading stage, using knurled-surface spacers and clamps. The stage was fixed into the SEM and the control cables were connected to the internal side of the flange. The strain gauge wires were also soldered to cables attached to the flange. On the outside of the SEM, a K&W Deformation Devices System (DDS) Multi-Level Controller was plugged into the flange with its own cables. Next, the EBSD camera was disconnected from the SEM and a National Instruments (NI) USB-6251 Digital/Analog Converter (DAC) system via a cable. The NI DAC was also connected to the
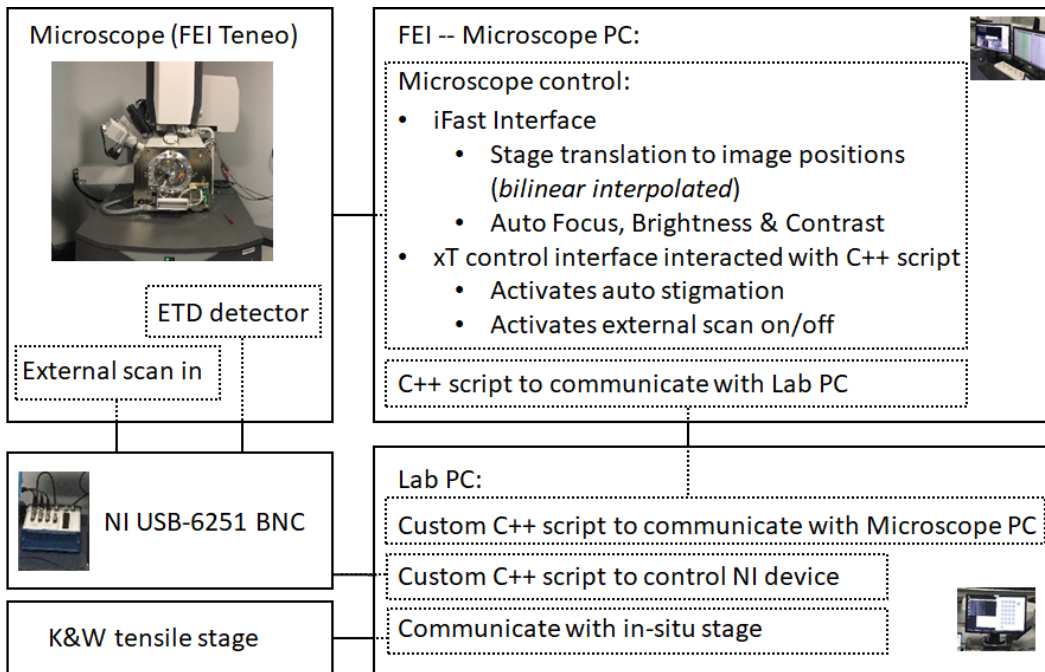
Figure 11. A diagram showing the systems required for external scan control. (Figure 5 from [16])

Per the guidelines for SEM-DIC (see Section 2.3.1), the image size and resolution should be chosen so that each nanoparticle is between 5x5 pixels and 7x7 pixels. For this reason, in order to image the 1x1mm AOI, square images of size 82x82μm and resolution 4096x4096 pixels were taken in a grid of 22x22 images. Each set of 484 images took approximately 24 hours to scan. A total of 1936 images were captured and analyzed for this test.

3.2.2 Scan Control Codes: iFast

The FEI Teneo SEM used for this work came equipped with iFast, a visual programming software that allows for automation of stage movement and imaging in the SEM. For the purposes of this experiment, an iFast script [29] [16] was used to control stage movement, and imaging parameters including focus, stigmatism, brightness, and contrast. The user inputs the coordinates of the

corners, the number of rows and columns, the desired image resolution and shape, and the naming convention (which is changed after each strain step to distinguish between them). Before starting, the user must position the stage such that the beam is centered on top left corner tile and the image parameters (focus, stigmatism, brightness, contrast) are as desired so that the iFast script has a starting point for reference.

When the program is run, the iFast code moves the stage to the initial coordinates, adjusts the image parameters, takes an image with the specified resolution, and then produces an audio tone to alert the external lab pc to start running the C++ code. The frequency of the audio tone is determined by the row and column number of the image being taken:

$$Frequency = 1000 + 100r + 4c \hspace{5cm} \text{Equation 9}$$

Where r = row number and c = column number.

3.2.3 Scan Control Codes: C++

When the audio tone is received by the external lab PC, images are captured by the methods described in Figure 5 in Section 2.3.2. The beam moves in a raster pattern and captures high-resolution images.

3.3 Monotonic Compression Testing

During the test described herein, the dogbone sample was loaded using a thermo-mechanical testing stage (Kammrath and Weiss) inside a FEI Teneo SEM, to three different strain levels, and

images were taken at each load: 0%, 0.8%, and 3%. The displacement rate was 0.1μm/s which, in this case, led to a quasi-static strain rate of 0.110,000=1x10^{-05}/s.
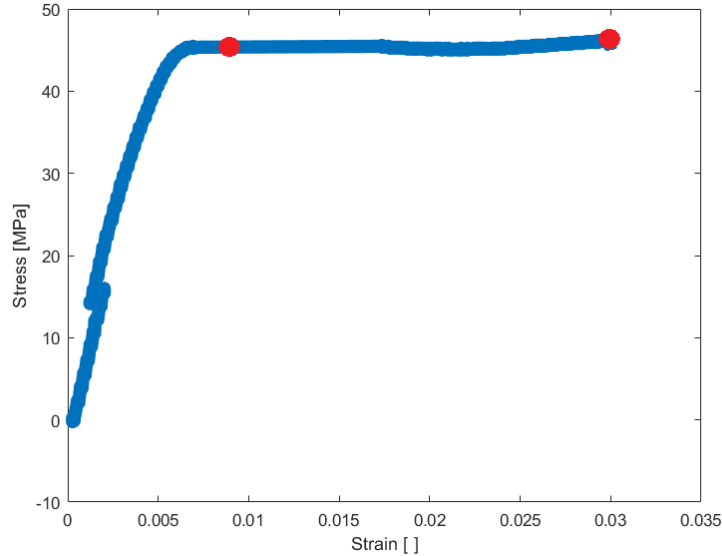
Figure 12. The stress strain curve for the test described herein. This curve has been edited to not include data from holding/imaging periods, during which stress-relaxation caused major dips in the curve. The blue line indicates the stress vs. strain data obtained from the stage and DDS controller. The red dots indicate the strains at which images were taken to be analyzed for this study. The discontinuity around 15MPa was caused by the opening of the SEM chamber and the tightening of the stage.

3.4 Data Processing

3.5.1 Digital Image Correlation

After the experiment, VIC-2D 6 by Correlated Solutions, Inc. (Irmo, SC) was used to perform the image correlation for this test. After some initial testing of processing parameters, a subset of 33μm and a step size of 3μm were chosen to minimize aliasing and maximize resolution of the DIC maps. A custom C++ script was used to run VIC-2D automatically for all 484 image tiles. After this

process was completed, several tiles which showed obviously false data were re-correlated individually using 9 seed points each. The deformation data of each tile were exported in matrices including the initial pixel positions, *x* and *y*, the displacement values, u and v, and the selected strain values (here, Lagrangian strains ε_{xx} ε_{yy} ε_{xy}).

3.4.2 Stitching [16]

After each image tile was analyzed with VIC-2D, a strain map of the entire AOI was created by stitching together the maps of each tile. There are several methods available for this work. A study by Carroll et al. in 2010 [13], which included stitching ex-situ images of tensile- and fatigue-crack growth experiments from an optical microscope, found that stitching the image tiles before performing DIC resulted in bands of artificial displacement/strain data that were non-negligible under 1% strain. Comparatively, performing DIC on each image tile and then stitching those DIC tiles together resulted in sharp strain discontinuities between tiles. The method used herein, developed by Chen et al. in 2018, utilizes the later strategy with additional steps to minimize these discontinuities. The first step in this process is to stitch together the reference SEM images.

First, the reference SEM images of each tile were stitched. This was done using MATLAB codes developed by Zhe Chen, which started by applying cross-correlation for image registration to find the stage position for each image. This cross-correlation is a measure of the similarity between two signals as a function of one signal's displacement relative to the other signal:

$$(F \circ G)(x,y) = \sum_{m=0}^{M-1} \sum_{n=0}^{N-1} F(m,n)G(m+x,n+y) \qquad \text{Equation 10}$$

$x \in [-(M-1), P-1]$, and $y \in [-(N-1), Q-1]$

Equation 6 represents the cross-correlation of an M-by-N matrix, F, and a P-by-Q matrix, G. These matrices represent the grayscale values of two SEM images. To estimate the noise in the cross-correlation, a first-order Savitzky-Golay filter with a window size of five was applied to smooth the data. This process allowed for the accurate evaluation of the stage position when each image was captured. Additionally, using the normalized cross-correlation can improve peak definition [31]:

$$\gamma(x,y) = \frac{\sum_{m,n}[g(m,n)-\bar{g}_{x,y}][f(m-x,n-y)-\bar{f}]}{\{\sum_{m,n}[g(m,n)-\bar{g}_{m,n}]^2 \sum_{m,n}[f(m-x,n-y)-\bar{f}]^2\}^{0.5}} \qquad \text{Equation 11}$$

g: image

f: template

$\bar{g}_{x,y}$: mean image under template

This cross-correlation algorithm was applied to each pair of neighboring image tiles and the common grayscale elements were identified. Thus, the position of each image tile was determined. In areas of the AOI where multiple tiles overlap at once, blending algorithms were used to stitch the tiles.

According to [16], there are several important considerations about the above-described stitching process:

1. Due to the computational cost of the cross-correlation (Eq. 10) it was optimized using the following cross-correlation theorem:

$$I \circ J = F^{-1}(\bar{F}(I)F(J))$$ Equation 12

The matrices I and J represent the grayscale values for two image, F is the forward Fourier transform, F^{-1} is the inverse Fourier transform, and the bar over F denotes the complex conjugate. Lewis [31] showed that Eq. 11 (normalized cross-correlation) can be converted into a cross-correlation that can be optimized by Eq. 12 and calculating terms involving the image sum and sum squared.

2. Computation time can be significantly reduced, if the image tiles are taken on a regular grid, if the relative tile positions are estimated before performing cross-correlation. This can be done using a subset of images in the estimated overlap area and will reduce the area to be searched for the cross-correlation peak. In the event that a solution cannot be found, manually selecting an image subset with distinctive features can also reduce the computational cost of the cross-correlation.

3. A perfect overlap of two neighboring images is impossible to produce, due to image distortion and noise. Figure 14 below shows an example of a region near the normalized cross-correlation peak for two images taken with the stock scan controller. The diagonal streak of high-value correlation points is caused by the spatial distortion discussed in Figure 6 in section 2.3.2. The peak represents the area with the most overlap of common

features.
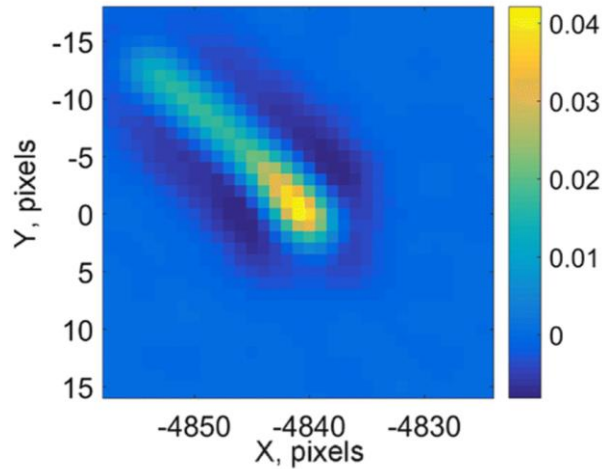
Figure 13. A region near the normalized cross-correlation peak for two images taken with the stock scan controller. The diagonal streak of high-value correlation points is caused by spatial distortions that cause common features to be captured differently between two images. This is discussed further in Figure 6 in section 2.3.2. (Figure 6 from [16])

4. In this experiment, and the one it is modeled after [16], the relative positions of the images were determined at pixel-resolution. Sub-pixel resolution was deemed unnecessary for these experiments due to the DIC step size being on the order of several pixels.

Once the correct positions of the SEM images were determined, those positions were used as a starting point for the DIC map tiles. The strain map tiles were stitched together to create a full-field, sub-micron resolution strain map of the full 1mm x 1mm AOI. The decision to perform DIC

and then stitch the maps had several motivations including distortion minimization and computational costs. In this experiment, the fully stitched image of the entire AOI is roughly 90,000 x 90,000 pixels (4096 x 4096 pixels for 22 x 22 image tiles). To create global matrices for each variable produced by VIC-2D 6 (x, y, u, v, ε_{xx}, ε_{yy}, and ε_{xy}), the local matrices for each image tile were stitched together. These global matrices describe the deformation data at evenly-spaced positions on the stitched reference image. The step size for these positions was equal to the DIC step size (here, 3):

$$X = \begin{bmatrix} 0 & 3 & 6 & ... \\ 0 & 3 & 6 & ... \\ 0 & 3 & 6 & ... \\ ... & ... & ... & ... \end{bmatrix} \text{ and } Y = \begin{bmatrix} 0 & 0 & 0 & ... \\ 3 & 3 & 3 & ... \\ 6 & 6 & 6 & ... \\ ... & ... & ... & ... \end{bmatrix}$$

The local matrices were inserted into the global matrix using the position of the relevant reference image in the global stitched reference image. For example, if a reference image tile was stitched to the global reference image starting at pixel position (n,m) and a data point in the local matrix is at position (x,y) then the same data point would be at ($n+x$, $m+y$) in the global matrix. In the event that ($n+x$, $m+y$) does not fall on a multiple of the step size, a nearest neighbor interpolation was applied and m and n were rounded to the nearest multiples of the step size. For example, using the step size of 3, (m,n)=(2,1) was rounded to (m,n)=(3,3). This process produced global matrices for each variable (x, y, u, v, ε_{xx}, ε_{xy}, and ε_{yy}) and is more accurate with smaller step sizes.

Stitching the strain fields in this way is fairly straightforward. The Lagrangian strain matrices were calculated using the displacement of itself and its four nearest neighbor data points, then smoothed using a Gaussian filter with filter size 5. Therefore, theoretically, the strain data should be the same in the overlap regions of different local matrices because strain is not affected by rigid translation. However, due to noise and distortion, this isn't always the case in practice. For this reason, the data in the overlay area with greater distortion (which, as discussed previously, occurs on the left

31

edge of right image tile) was discarded and only the data from the low-distortion matrix (the right side of the left matrix being stitched) was used (see Figure 6 in section 2.3.2 (the one with the left edge distortion)). In the case where image distortion was relatively even between the image tiles, an average of the overlap data was used in the global matrix.

Stitching displacement matrices was more complicated than stitching strain matrices, because by definition they are impacted by rigid body translation. So, before being able to insert the local displacement matrices in the global displacement matrices, certain calculations were necessary as follows:

Say that a trackable feature is imaged at position (x_i, y_i) on the reference image tile and at (x_f, y_f) on the deformed image tile. The displacement values would be:

$$(u', v') = (x_f - x_i, y_f - y_i) \qquad\qquad \text{Equation 13}$$

The tile in which this trackable feature lies starts at position (x_r, y_r) in the reference stitched image and at (x_d, y_d) in the deformed stitched image. Therefore, the feature in question lies at (x_r+x_i, y_r+y_i) in the stitched reference image and at (x_d+x_f, y_d+y_f) in the stitched deformed image. Thus, for the global matrices, the displacement values are:

$$(u, v) = ((x_d + x_f) - (x_r + x_i), (y_d + y_f) - (y_r + y_i)) \qquad\qquad \text{Equation 14}$$

$$= (u' + (x_d - x_r), v' + (y_d - y_r))$$

Therefore,

$$u' = u - (x_d - x_r)$$

Equation 15

$$v' = v - (y_d - y_r)$$

Equation 16
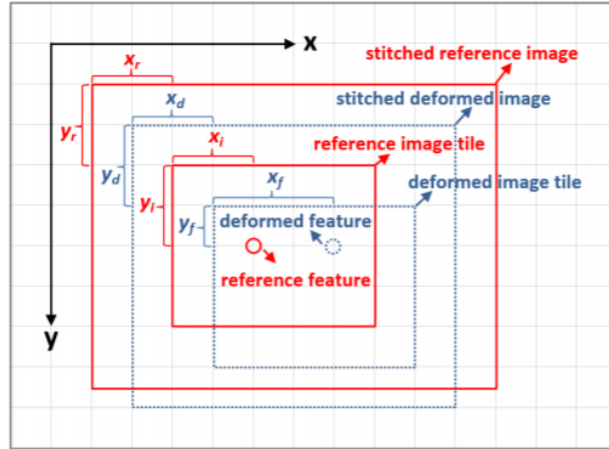
Figure 14. An illustration of the relationships between displacement in local matrices (reference and deformed) and the global displacement matrices (reference and deformed). The solid red lines represent a reference image tile and the stitched reference image. The blue dotted lines represent a deformed image tile and the stitched deformed image. The circles represent trackable features in the reference images (red) and the deformed images (blue). The position of the feature in the image tile are shown: (x_i, y_i) on the reference image tile and at (x_f, y_f) on the deformed image tile. The position of the image tile in the stitched image are also shown: (x_r, y_r) in the reference stitched image and at (x_d, y_d) in the deformed stitched image. Eq 10 shows the relationships between these position values and the displacement of the feature in the global stitched image. (Figure 7 from [16])

As shown in Eqns 11 and 12, the displacement of each feature in a tile depends on the position of its image tile in the global image, (x_r, y_r) and (x_d, y_d). In overlap areas, features' displacements are different because the positions of their respective image tiles are different. This leads to a discontinuity in the stitched area, as can be seen in Figure 15.(a), where data from the left image was used in the left have of the overlap area and data from the right image was used in the right half of the overlap area. To get rid of this discontinuity, Eq. 14 was used to correct the values in the local matrices such that the displacement fields in different local matrices become the same in the overlap region. (x_d-x_r) and (y_d-y_r) were added to u' and v', the local displacement matrices, when stitching, which corrected the discontinuity as shown in Figure 15(b).
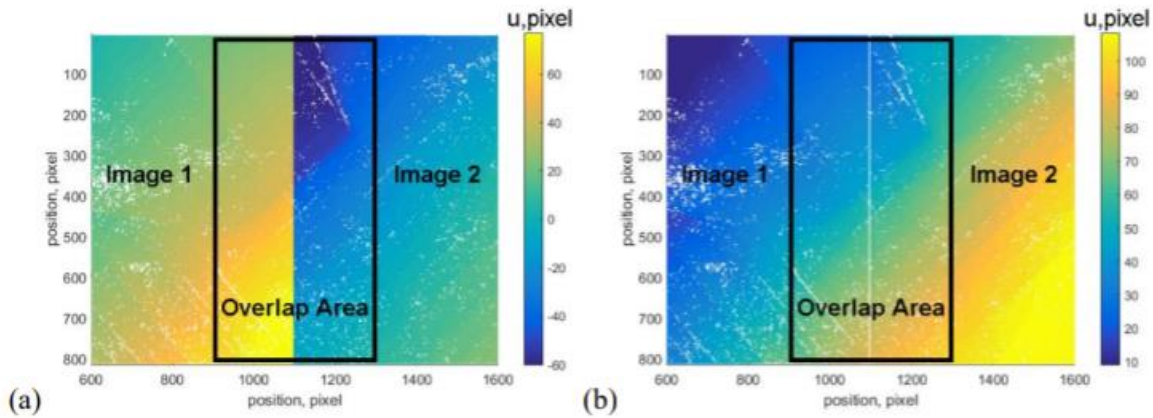
Figure 15. When stitching local displacement fields, the data must be corrected to avoid discontinuities caused by the relationship between displacement and position in the global matrix. (a) A discontinuity is evident in the overlap are, where data from image 1 was used in the left half of the area and data from image 2 is used in the right have of the area. (b) When the data is corrected using Eq. 14 the discontinuity is corrected. (Figure 8 from [16])

Figure 16 shows the full-field strain maps, comprised of 484 (22 rows x 22 columns) data tiles stitched together using the methods described above. The macroscopic strain was approximately 3% and the step size between data points is 3 pixels. This corresponds to approximately $\frac{82 \mu m}{4096\ pixels} \times 3\ pixels = 0.06 \mu m$. Both slip and twinning can clearly be identified in Figure 16.

34
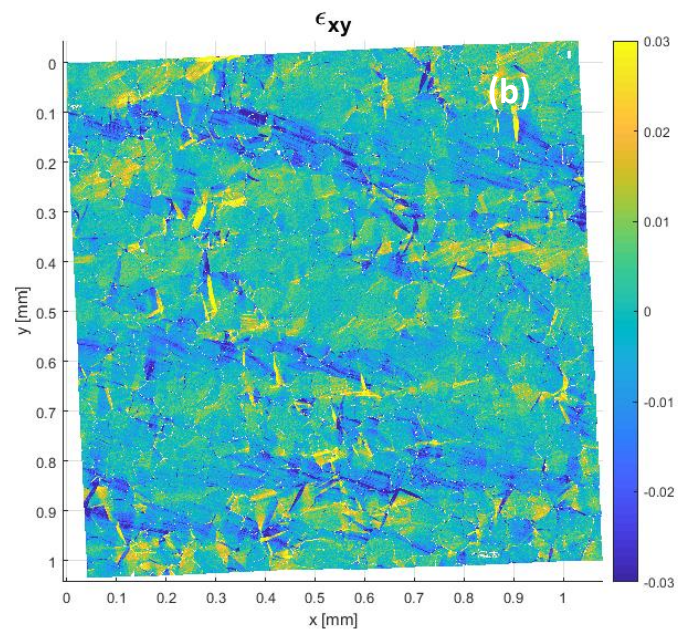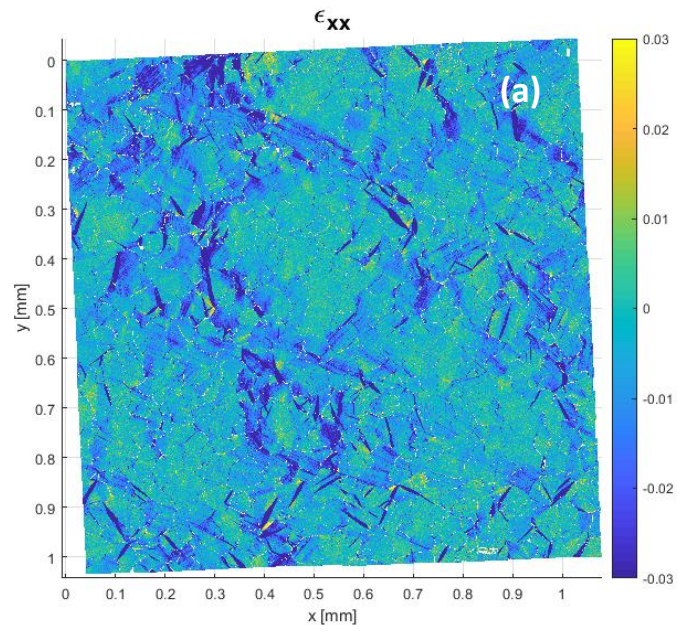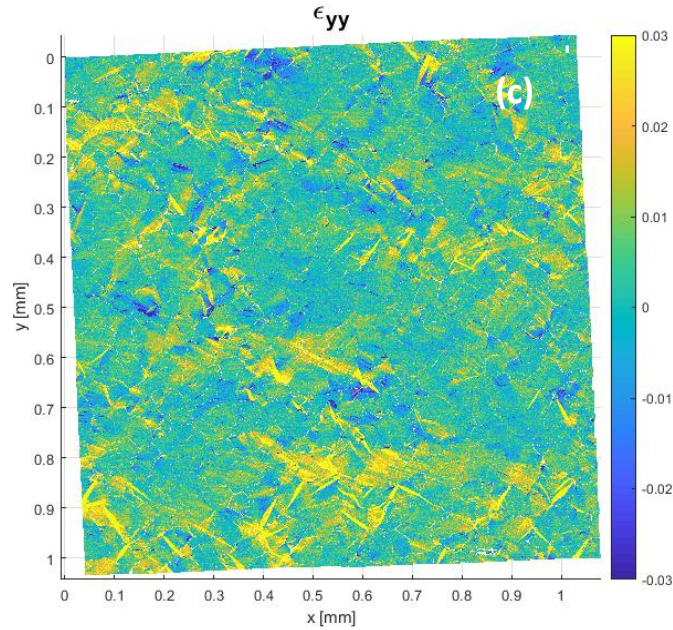
Figure 16. The (a) ε_{xx}, (b) ε_{xy} and (c) ε_{yy}, stitched strain maps for the full area of interest under global strain of approximately 3%, calculated using Vic-2D 6.

3.4.3 Aligning Strain and Microstructural Data [16]

To relate the strain data with the microstructural information from EBSD, the full-field strain map was aligned with the grain orientation map. The EBSD is more inherently distorted, so the EBSD data was aligned to the DIC coordinate system rather than the other way around. To do this, a projective transformation was used.

The projective transformation [16] used works by matching lines in the EBSD data to lines in the DIC data, but it does not necessarily retain parallelism. For each the EBSD map and the DIC data map, N control points were chosen. Their positions defined as (x_i, y_i) on the EBSD map and (X_i, Y_i) on the DIC map, where $i \in [1, N]$. A 3-by-3 matrix, H, can be used to represent the projective transformation, where

$$H = \begin{bmatrix} h_1 & h_4 & h_7 \\ h_2 & h_5 & h_8 \\ h_3 & h_6 & h_9 \end{bmatrix}$$

Equation 17

Here, $h_9=1$, and the control points satisfy the following relationships:

$$X_i = \frac{x_i h_1 + y_i h_2 + h_3}{x_i h_7 + y_i h_8 + h_9}$$

Equation 18

$$Y_i = \frac{x_i h_4 + y_i h_5 + h_6}{x_i h_7 + y_i h_8 + h_9}$$

Equation 19

Expanding these relationships for all N control points:

$$\begin{bmatrix} X_1 \\ Y_1 \\ X_2 \\ Y_2 \\ \dots \\ X_n \\ Y_n \end{bmatrix} = \begin{bmatrix} x_1 & y_1 & 1 & 0 & 0 & 0 & -X_1 x_1 & -X_1 y_1 \\ 0 & 0 & 0 & x_1 & y_1 & 1 & -Y_1 x_1 & -Y_1 y_1 \\ x_2 & y_2 & 1 & 0 & 0 & 0 & -X_2 x_2 & -Y_2 y_2 \\ 0 & 0 & 0 & x_2 & y_2 & 1 & -X_2 x_2 & -Y_2 y_2 \\ \dots & \dots & \dots & \dots & \dots & \dots & \dots & \dots \\ x_n & y_n & 1 & 0 & 0 & 0 & -X_n x_n & -Y_n y_n \\ 0 & 0 & 0 & x_n & y_n & 1 & -X_n x_n & -Y_n y_n \end{bmatrix} \begin{bmatrix} h_1 \\ h_2 \\ h_3 \\ h_4 \\ h_5 \\ h_6 \\ h_7 \\ h_8 \end{bmatrix}$$

Equation 20

Or:

$Q=PA$ Equation 21

This system of linear equations (Eq. 20) becomes overdetermined in the case where $N > 4$. Therefore, matrix A was solved by the generalized inverse to average the effect of more than four control point pairs:

$A=(P^TP)^{-1}P^TQ$ Equation 22

Eq. 22 provided all the required elements to define the transformation of matrix H.

After the data was run through the projective transformation, the grain boundaries were manually adjusted in areas where the transformation was not completely successful. As the EBSD data has increased distortion compared to the DIC data, the DIC data was used to make these adjustments. The grains around the edge of the AOI were omitted due to incomplete microstructural data (grain size could not be calculated from only part of a grain.)

The combined EBSD and DIC map can be seen in Figure 17.
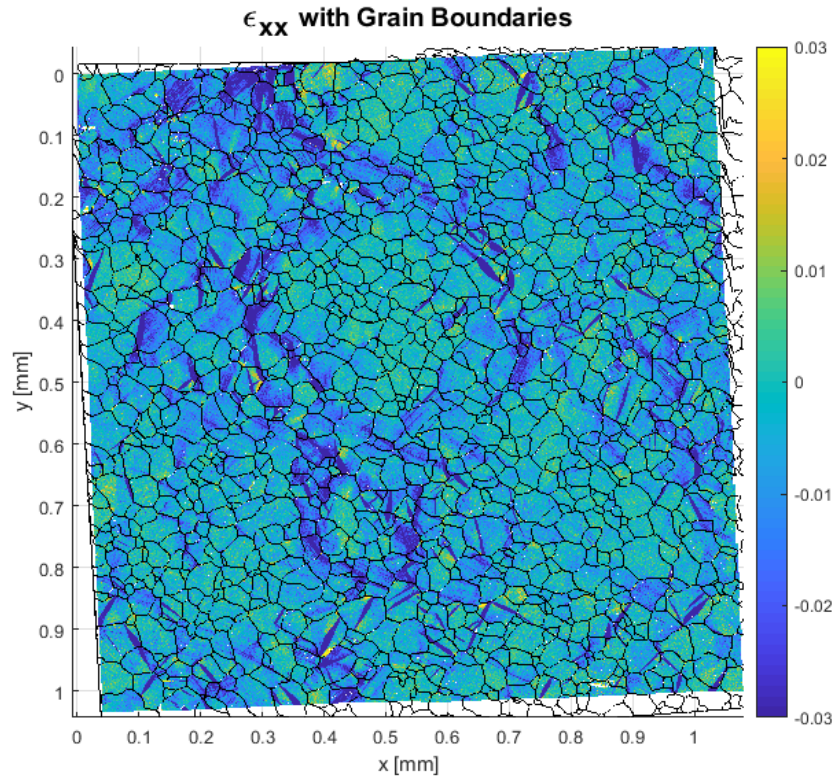
Figure 17. The ε_{xx}, strain map (Figure 17.), overlaid by the grain boundaries found using the EBSD data (Figure 9). For some grains near the edges, that either did not have full EBSD or DIC data could not be examined as a part of this investigation.

3.4.4 Twin Identification [15]

Once the EBSD data and the DIC data were combined so that the strains in individual grains could be studied, the next step towards the goal of comparing twinning and grain size was to identify the twins present in each grain. Computer vision and machine learning techniques, developed by Chen and Daly in 2018 [15], were used to identify twins in three steps: K-means clustering of the strain data, comparing the experimentally recorded strains in those clusters to theoretical twinning strains combined with twin system Schmid Factors, and examining cluster shape and size evolution using

a Convolution Neural Network (CNN). These processes are described below, but for more details the reader is directed to [15].

3.4.4 (a) Segmentation of Deformation Data: K-Means Clustering

As developed in Chen and Daly [15] the following was used to segment strain so that twins can be identified and examined: First, k-means clustering was applied to the strain fields of each grain in the R^3 space of $\{\varepsilon_{xx}, \varepsilon_{xy}, \varepsilon_{yy}\}$. The number of clusters in each grain, $K \in [2,5]$ was found such that the averaged silhouette value $\bar{S}$ (Eq. 23) was maximized.

$$\bar{S} = (\sum_i S(i))/N \hspace{4cm} \text{Equation 23}$$

The silhouette is a measure of how well a data point fits the cluster to which it is assigned, compared to other clusters. It can vary between -1 and 1, and it can be calculated using Eq. 24.

$$S(i) = \frac{b(i)-a(i)}{\max\{a(i),b(i)\}} \hspace{4cm} \text{Equation 24}$$

where *i* represents the data point being examined, *a(i)* is the average distance between *i* and the other data in the same cluster, and *b(i)* is the average distance between *i* and the data in the next closest cluster. In each grain, silhouette values were calculated for 10,000 uniformly distributed data points, rather than the entire data set, as to cut down on computational costs. The resulting clusters for all 1292 grains can be seen in Figure 18. The sliver of missing data is an artifact of

stitching the strain data and correlates to an area where sigma (a measure of the quality of the DIC calculations produced by Vic-2D) was equal to zero.
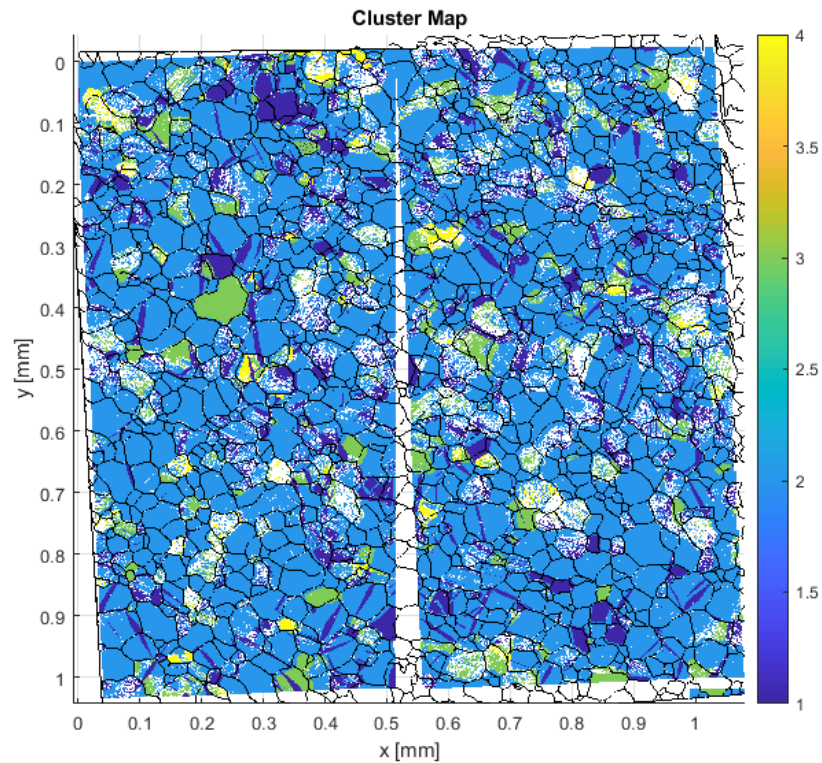
Figure 18. This map shows the results of the k-means clustering for the entire AOI. The white areas are areas where sigma=0, according to Vic-2D 6.

This twin segmentation method can be further improved, however. About 1-2% of twins are not segmented separately from their parent grains, and some areas of high strain that happen to have similar strains are a twin can be mistakenly segmented into a twin cluster. To improve upon the results from k-means clustering alone, the examination of theoretically expected twin strains, cluster size evolution, and cluster shape was undertaken.

3.4.4 (b) Comparison of Theoretical and Experimental Strains, Combined with Twin System

Schmid Factors

As developed in Chen and Daly [15], the following was used: to find whether a given cluster corresponded to a twinned or parent area, the centroid of each cluster was compared with the theoretical surface strain values for the most likely twin systems. In VIC-2D, the Lagrangian strain fields were determined by:

$$\varepsilon = \frac{1}{2}(\boldsymbol{F}^T\boldsymbol{F} - \boldsymbol{I})$$

Equation 25

where $\boldsymbol{F}$ is the deformation gradient:

$$\boldsymbol{F} = \boldsymbol{I} + \frac{\partial \boldsymbol{u}}{\partial \boldsymbol{X}}$$

Equation 26

$\boldsymbol{I}$ is the identity tensor, $\boldsymbol{u}$ is the displacement, and $\boldsymbol{X}$ is the position of the material point before deformation. For 2D-DIC, the experimental data falls on the x_1-x_2 plane and the strain components are $\{\varepsilon_{xx}, \varepsilon_{xy}, \varepsilon_{yy}\}$. This leads to: $\boldsymbol{u} = (u_1, u_2)$ and $\boldsymbol{X} = (x_1, x_2)$. The deformation gradient for a given twin system α can be calculated using Eq. 27:

$$\boldsymbol{F} = \boldsymbol{I} + \gamma^\alpha(\boldsymbol{B}\otimes\boldsymbol{N}) = \boldsymbol{I} + \gamma^\alpha \begin{bmatrix} b_1 n_1 & b_1 n_2 & b_1 n_3 \\ b_2 n_1 & b_2 n_2 & b_2 n_3 \\ b_3 n_1 & b_3 n_2 & b_3 n_3 \end{bmatrix}$$

Equation 27

where γ^α is the twin shear, $\boldsymbol{B} = (b_1, b_2, b_3)$ is the twinning direction, and $\boldsymbol{N} = (n_1, n_2, n_3)$ is the twinning plane normal. $\boldsymbol{B}$ and $\boldsymbol{N}$ are 3D crystallographic characteristics that were measured with

2D-DIC. Therefore, b_3 and n_3 could not be determined and the deformation gradient in this case was calculated as:

$$\boldsymbol{F} = \boldsymbol{I} + \gamma^\alpha \begin{bmatrix} b_1 n_1 & b_1 n_2 \\ b_2 n_1 & b_2 n_2 \end{bmatrix}$$

Equation 28

To calculate the theoretically-predicted surface strains as measured in experiment, Eq. 28 was substituted into Eq. 25. Assuming that deformation twins were the sole contributor to shear strain in twinned areas, this theoretical strain was expected to match the experimentally-determined strain fields from 2D-DIC.

For each grain, the centroid of each cluster was compared with the theoretically-predicted surface strains for all six extension twin variants in that grain. A dissimilarity metric (ψ^D) between the experimental and theoretical strains was determined using a Euclidean distance:

$$\psi^D(n) = \sqrt{\Sigma(\varepsilon_{ij}^{cluster} - \varepsilon_{ij}^{Twin(n)})^2} \; , n \in [1,6]$$

Equation 29

where n is one of the six available extension twin systems, $\varepsilon_{ij}^{cluster}$ is the experimentally obtained centroid of the strain in the cluster, and $\varepsilon_{ij}^{Twin(n)}$ is the surface strain predicted for twin system n. Whichever of the six twin systems exhibited the minimum dissimilarity (ψ_{min}^D) with the cluster strains was assigned as the cluster's potential twinning system. This was done with no knowledge of whether the cluster had twinned or not.

$$\psi_{min}^D = \min\{\psi^D(n)\}, n \in [1,6] \hspace{4cm} \text{Equation 30}$$

Note that there is a limitation with this approach of assigning potential twin systems to clusters; two twin systems could exhibit very similar twinning strains. This is further discussed in [15].

Clusters with low dissimilarity (ψ_{min}^D) and high Schmid factors (m) are more likely to be twinned, because these characteristics indicate that the exhibited strain is very close to the theoretically-predicted surface strain for a twin system and that the orientation of the grain within which the cluster resides is well-oriented for that twin system to be subjected to high resolved shear strain. For this reason, Chen and Daly [15] found that, when examining the relationship between dissimilarity and Schmid factor, the likely twinned clusters tended to congregate in a region of high m and low ψ_{min}^D (top left corner in Figure 19.) The twin identification (and therefore color difference) are a result of twin identification work discussed later.
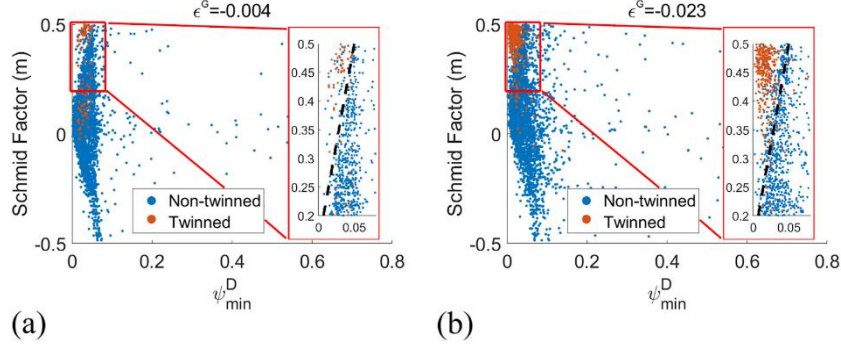
Figure 19. Scatter plots of dissimilarity (ψ_{min}^D)) vs. Schmid factor (*m*) for (a) ε^G = -0.004 and (b) ε^G = -0.023. The region in the top left corner, containing most of the likely-twinned clusters (orange), represents areas of high Schmid factor and low dissimilarity, and also shows the fact that lower *m* values can be offset by a lower ψ_{min}^D) while a higher ψ_{min}^D) could be offset by a higher *m* to form twins. The twin identification (and therefore color difference) are a result of twin identification work discussed later. (Figure 6 from [15])

The linear boundary between the twinned and non-twinned regions can be approximated as follows:

$$B = m - c\psi_{min}^D \qquad \text{Equation 31}$$

where *c* is the slope of the boundary, and *B* is the intersection of the boundary with the Schmid factor axis. In the work done by Chen and Daly [15] it was found that *c* = 7 and *B* = 0.15.

Next, a classifier (φ) was defined as:

$$\phi = \frac{1}{1+c}(m - c\min\{\psi_{min}^D, 1\}) + \frac{1+2c}{2(1+c)} \qquad \text{Equation 32}$$

$$= \frac{1}{1+c}m - \frac{c}{1+c}\min\{\psi_{min}^D, 1\} + \frac{1+2c}{2(1+c)}$$

45

ϕ allows for examination of the potential delineation of B. This classifier maintains the linear relationship between ψ^D_{min} and m with the following boundaries:

$$\begin{cases} \phi(n = 0.5, \psi^D_{min} = 0) = 1 \\ \phi(n = 0.5, \psi^D_{min} = 1) = 0 \end{cases} \qquad \text{Equation 33}$$

This makes the lower bound zero in Eq. 33 and caps the dissimilarity at 1. In Figure 19 it can be seen that all clusters have $\psi^D_{min} < 1$, so the following relationship is satisfied:

$$\phi = -\frac{1}{1+c}B + \frac{1+2c}{2(1+c)} \qquad \text{Equation 34}$$

This shows that ϕ is a linear mapping of B into the interval $[0,1]$ and φ represents the likelihood that a cluster has twinned. Given an estimate for c (in [15] c was approximated as 7), ϕ can be calculated for each cluster, and clusters with $\phi > \phi_{th}$ (where ϕ_{th} is a set threshold likelihood value) can be classified as twinned. ϕ_{th}, however, will vary between materials, samples, and tests, and at this stage is just a starting point for grouping like clusters into "twinned" or "not twinned." The threshold value used for data analysis in this study was ϕ_{th}=0.95. Figure 20 shows the results of the above-described process for the strain data in this study.
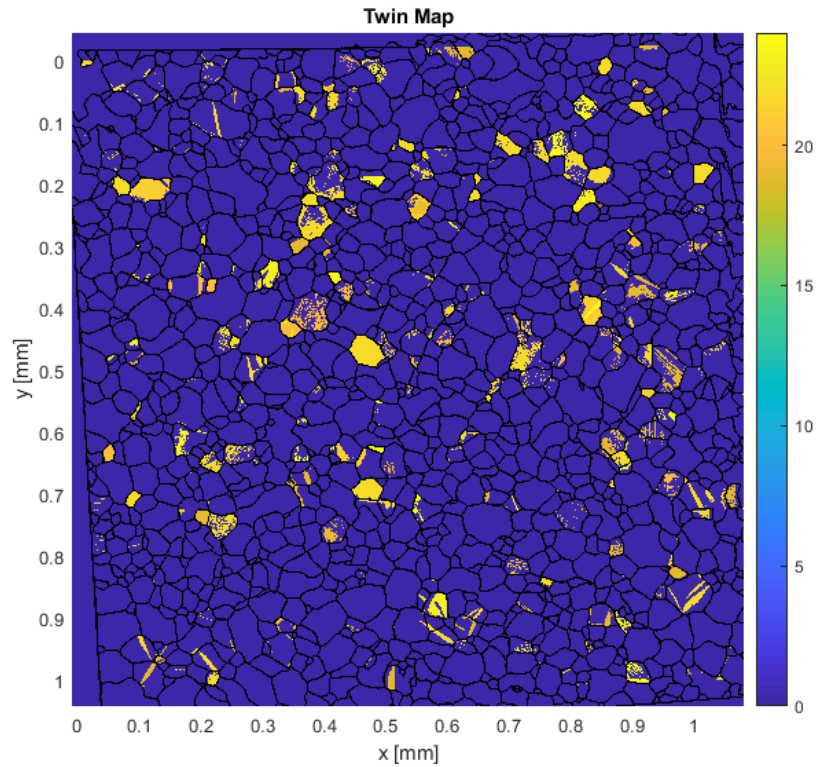
Figure 20. The yellow highlighted clusters in this map of the full AOI indicate clusters predicted to be probable twins by the methods described in this section: these clusters display strains consistent with theoretically-predicted strains for twins in the same grains. In this case, these identified twins correspond to clusters where $\varphi>0.95$.

3.4.4 (c) Cluster Size Evolution and Cluster Shape Identification

As developed in Chen and Daly [15], the following was additionally used to separate likely-twinned clusters from likely-not-twinned clusters by examining their shapes and investigating how their sizes change as strain increases. These characteristics are useful in identifying twins because 1) under monotonic loading, twins will only grow, they will not shrink in size; and 2) when twins nucleate, they have a distinct thin, lenticular shape. These measures cannot, however, prove whether a cluster is a twin or not, because areas of slip may also grow and/or take on long thin shapes; rather, investigating the size and shape of clusters was to inform the previous methods used for twin identification.

Cluster size, in pixels, was applied first in an effort to identify twinned clusters. In the k-means calculations discussed in Section 3.4.4 (a), cluster IDs were assigned at random. This means that the first step in investigating size change was to link the cluster IDs between strain steps, to ensure the correct cluster was being examined at each strain step. To do this, the total overlap in pixel count between the clusters at the two strain steps was maximized. This was repeated for every group of clusters in every grain in the AOI, and a significant increase in size was evident for twinned regions while a decrease in size was evident for non-twinned regions. Figure 21 shows an example of a single grain, with its strain clustered, and the corresponding cluster sizes in pixels.
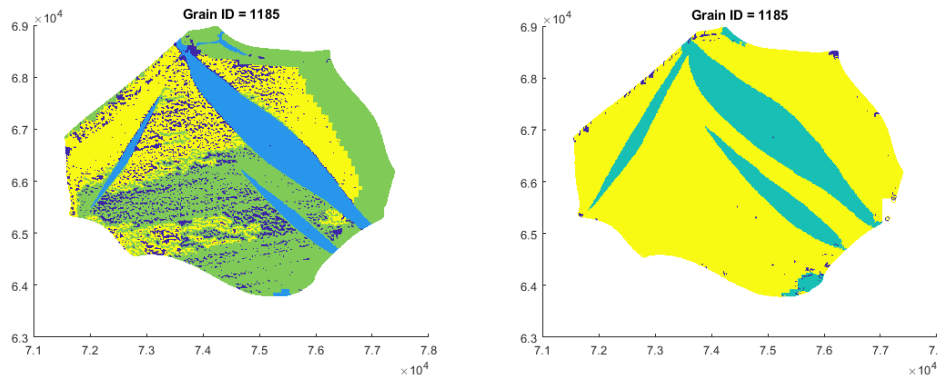
Figure 21. As an example of how twin clusters grow with increased strain, the clusters in Grain #1185 is plotted. The twin cluster (blue in (a) and teal in (b)) grows from ~82,000 pixels to ~124,000 pixels between strains (a) $\varepsilon_{xx} \cong 0.8\%$ to (b) $\varepsilon_{xx} \cong 3\%$.

	Global Strain	Cluster Size [pixels]
(a)	0.80%	81,654
(b)	3%	123,813

48

Table 1. The corresponding cluster size data for the
twinned cluster in grain 1185 in Figure X.

The cluster size growth ratio (*r*) was defined for loading step *n* as follows:

$$r(n) = \frac{S(N) - \min\{S(i)\}}{G}, i < n$$ Equation 35

where $S(i)$ is the cluster size at strain step *i*, *N* is the final load step being examined, and *G* is the

number of pixels inside the cluster's parent grain. $r \in [-1,1]$ and represents the increase or

decrease in cluster size depending on strain step. From *r(n)*, another parameter P_{size} was defined

as:

$$P_{size}(n) = \frac{r(n) + 1}{2}$$ Equation 36

where P[0,1] and represents the probability that a cluster is twinned at step *n*, based on the

evolution of its size. This probability was calculated for each cluster in each grain to help identify

twinned regions.

For the cluster shape characterization, strain clusters were converted to images and the MATLAB

Neural Network Toolbox was used to apply transfer learning to the cluster images. Next, a pre-

trained AlexNet Convolution Neural Network (CNN) [27] was configured to learn and perform

classification into two classes, 'twin' and 'non-twin'. The last three layers of this CNN were

of 227x227 by using x- and y-dimension down-sampling with the same step size, so the aspect ratio of the grain remained the same. Data outside the border of the new smaller dimensions were padded with NaNs. Linear interpolation was used to convert each strain map into the red, green, and blue channels of an RGB image. Based on theoretical surface strain predictions and the experimentally-measured strain distribution across the entire AOI, strains were mapped to the RGB values as follows:

ε_{xx} [− 0.14, 0.07] → R[0,225], ε_{xy} [− 0.07, 0.07] → G[0,225], ε_{yy} [− 0.07, 0.14] → B[0,225]

Once the entire grain was converted into an RGB image, individual cluster-specific images were created wherein each image contained only pixels from one cluster. 4,811 images were generated for all strain steps using this method.

150 images were used for training the CNN, 50 for 'twin' and 150 for 'non-twin.' Furthermore, these images were divided into (a) images for training and (b) images for validation. To train the CNN, the loss function of the classification layer was minimized. This minimized the difference between the predicted and validation classification labels during training. *E*, the cross-entropy loss function of a type commonly applied to neural networks, was applied to the CNN and is defined as:

$$E = - \sum_{i=1}^{n} \sum_{j=1}^{k} y_{ij} \ln(p_{ij})$$
<div align="right">Equation 37</div>

where *n* is the number of observations, *k* is the number of classes, y_{ij} is a binary indicator for observation *i* belonging to class *j*, and p_{ij} is the predicted probability from the previous layer that

observation *i* belongs to class *j*. The training process was terminated when the loss on the validation data set was larger than the smallest loss for the previous five steps.

Once trained, the CNN was used to classify all clusters in all grains in the AOI. Along with classifying each cluster, the CNN produced an activation value for the classification layer for each cluster. This activation value can be interpreted as the probability $p(i)$ that the cluster in question corresponds to a twinned region. To determine whether a cluster was a twin, the maximum $p(i)$ value for a cluster and its linked clusters from all previous strain steps was used:

$$P_{CNN}(n) = \max\{p(i)\}, i \leq n \qquad\qquad \text{Equation 38}$$

Figure 22 shows the resulting twin map produced by the trained CNN.
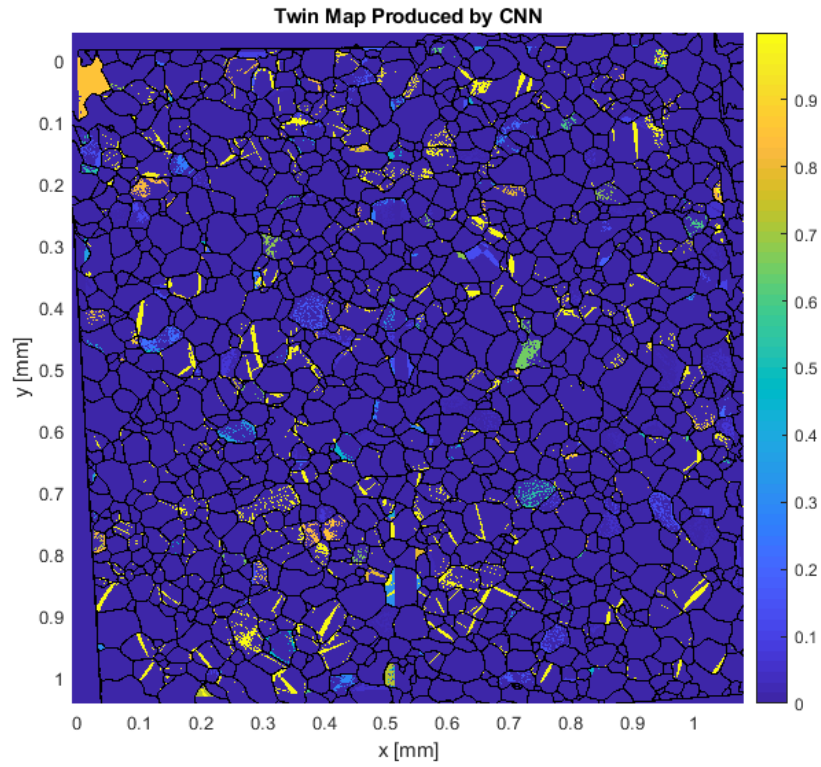
Figure 22. The resulting twin map produced by the trained CNN.

P$_{size}$ and P$_{CNN}$ (Eqns 32 and 34) were then combined and a new classifier was defined to represent the probability that a given cluster was a probably twin, using both size evolution and shape identification criterion:

$$\eta = P_{size} \times P_{CNN}$$ Equation 39

P$_{size}$ and P$_{CNN}$ are independent characteristics of a cluster; whether the cluster grew or shrank does not change whether the shape of the cluster resembled that of a twin, and vice versa. $\eta > \eta_{th}$

indicates that a cluster is likely twinned. In this case, η_{th}=0.5075. This was used when

combining all methods from 3.4.4 (a), (b), and (c) in section 3.4.4 (d).

3.4.4 (d) Combining Twin Identification Methods

The final step of these data analysis methods developed in [15] was to combine the theoretical

strain analysis, the CNN analysis, and the size evolution analysis to identify twins in the AOI.

Figure 23. shows the resulting clusters identified as likely twins using the combination of all of

these methods. The way this was done was by using a logical OR relationship between the $\phi >$

ϕ_{th} criterion for investigating the experimental strains as compared to the theoretically predicted

strains, and the $\eta > \eta_{th}$ criterion, which combines size evolution and shape identification to

analyze clusters' probability of corresponding to a twin.
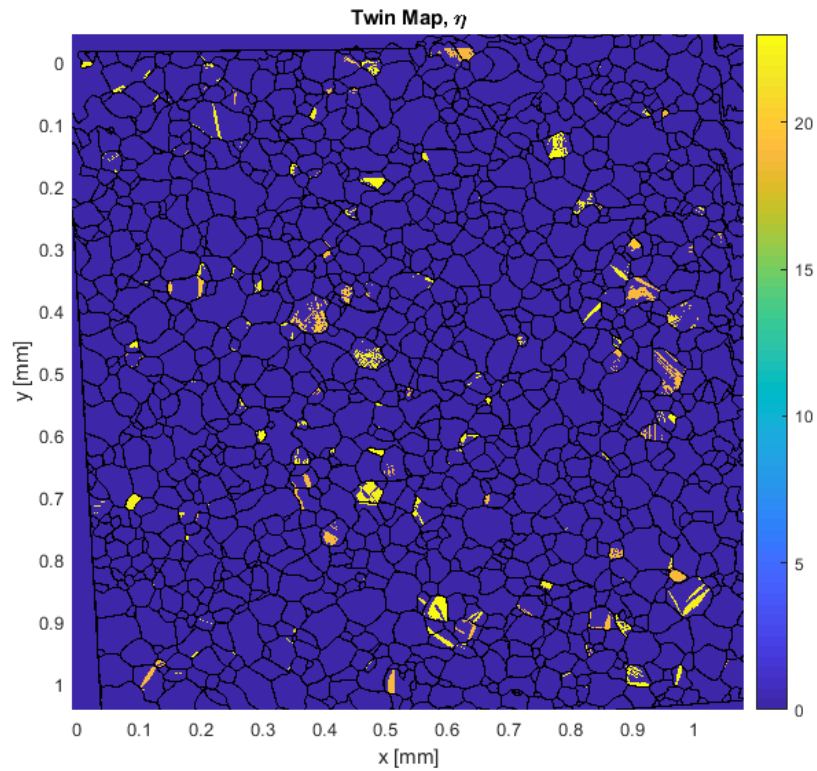
Figure 23. This twin map was produced by combining the assessment of the experimental strains to the theoretical strains with the examination of the cluster size evolution and the cluster shapes. The yellow highlighted regions correspond to areas that have φ >0.95 OR >0.5075.

3.4.5 Capturing Ground-Truth Data

The methods for analyzing the data described in section 3.4.4 are still in development and cannot yet identify twins in DIC data with 100% accuracy. For this reason, the identification of a ground-truth data set was required. To capture this ground-truth data, the strain map for each grain in the AOI was plotted and categorized by hand. If the grain included a twin, the grain ID number was recorded, and the conclusions drawn in the following sections were made using this information.

3.4.6 Precision, Sensitivity, and Accuracy

By comparing the predicted data (section 3.4.4 (d)) and the ground-truth data (section 3.4.5), the following automated identifications were determined. The high prevalence of false negatives is likely due to the high level of noise in the experimental data, as evidenced in Figure 21.

True Positive	65
False Positive	134
True Negative	1043
False Negative	54

Table 2. The results of comparing the grains predicted to include twins with the ground truth data of which grains actually do include twins. "True" indicates correct predictions, "false" indicates incorrect predictions, "positive" indicates grains with twins, and "negative" indicates grains without twins.

The "true positive" (TP) value corresponds to grains that were correctly predicted to have twins, the "false positive" (FP) value represents the grains that were wrongly predicted to include twins, the "true negative" (TN) value is the number of grains that were correctly predicted to include no twins, and the "false negative" (FN) value represents the grains that were incorrectly predicted to contain no twins. These results were used to calculate three metrics, previously defined in [15]: 1) Precision or Positive Predictive Value (PPV), 2) Sensitivity or True Positive Rate (TPR), and 3) Accuracy (ACC). Each of these values is a ratio between TP, TN, FP, and/or FN.

The PPV is a ratio of the predicted twinned grains to the total positive predictions:

$$PPV = \frac{TP}{TP+FP}$$
<div style="text-align: right">Equation 40</div>

The TPR is the ratio between the correctly predicted twinned grains and the total actual positive observations:

$$TPR = \frac{TP}{TP+FN}$$

Equation 41

The ACC is the ratio between the correct predictions and the total observations:

$$ACC = \frac{TP+TN}{TP+FP+TN+FN}$$

Equation 42

The results of these metrics are in Table 3.

PPV	0.326633166
TPR	0.546218487
ACC	0.854938272

Table 3. The precision (PPV), sensitivity (TPR), and accuracy (ACC) were calculated using Eq. 40, 41, and 42

As shown in Table 3, the precision of ~33% is relatively low, as is the sensitivity of ~55%. The accuracy is higher, at ~85%, but still too low to draw significant conclusions. The methods described herein severely over-predicted twins, with almost twice as many FP values as TP values. To improve upon these statistics, several improvements to the process could be made. These

include higher-quality test data, different clustering techniques, and a better neural network which has been trained over several tests on several samples to identify twinned clusters.

IV. Results and Discussion

The goal of this work was to identify a relationship between the occurrence of twins in a grain and the size of that grain (*d*). Figure 24 shows the results of this investigation, using the ground-truth data categorized manually. The grain size values used are surface grain sizes and were calculated using the TSL OIM Analysis software. It can be seen that, with a few exceptions, the percentage of grains exhibiting twins is greater as the average grain size increases. Note, however, that the statistical significance of these results greatly reduces when the grain size increases past nominally 1500 μm^2, as the number of grains is significantly decreased (Figure 24(a)).
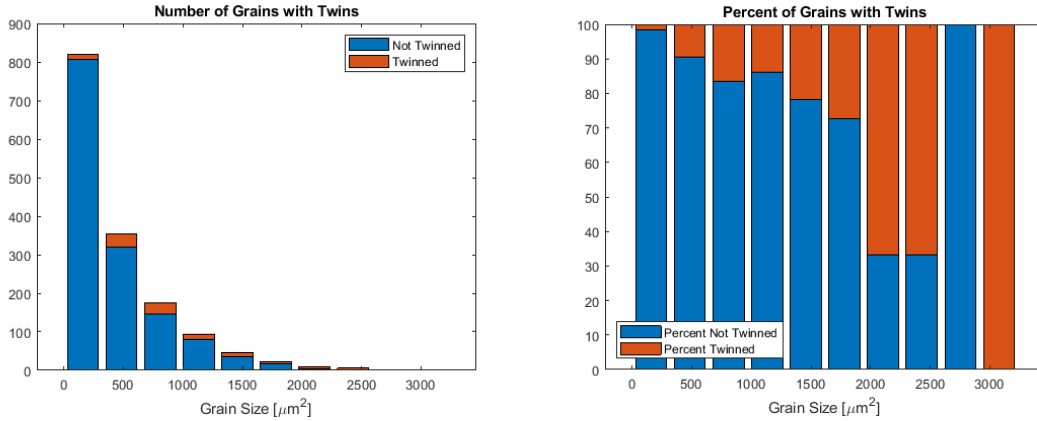
Figure 24. (a) The raw count of grains that twinned (orange) and that did not twin (blue). Most grains did not twin and fell into the smallest size category: 0<d<323.8. (b) The percentage of grains that exhibited twins (orange) increased with grain size.

One notable outlier comes from grain sizes of $2428\mu m^2 < d < 2752\mu m^2$ (the all-blue column in Figure 24. (b)). Note that this group and the final one ($2752 \ \mu m^2 < d < 3076 \ \mu m^2$) each only include one grain, therefore rendering those groups statistically insignificant. Testing multiple samples of multiple average grain sizes under the same conditions would increase the sample size for each grain size grouping and improve the accuracy of these results.

Deformation mechanisms in magnesium (and other HCP materials) include basal (<a>) slip, non-basal (<c> or <c+a>) slip, and twinning. These different mechanisms have drastically different critical resolved shear stresses (CRSS) due to the asymmetry of the HCP crystal structure. The primary deformation mechanism in magnesium, basal slip, has the lowest CRSS (because it occurs on the closest-packed plane) and nearly always occurs, while the secondary mechanisms, non-basal slip and twinning, have higher CRSS values and only occur when conditions are adequate (though one or the other must occur in order to accommodate arbitrary deformation).

As stated in Section 2.2, the reasons that twinning is likely to dominate as a secondary deformation system in larger grains are not yet fully understood. Wang et. al [49] asserted that the probability

Magnesium and its alloys are of great interest to the structural materials community due to their high strength-to-weight ratio as compared to other structural materials. However, their low ductility and the relative lack of knowledge surrounding their failure mechanisms has lead to a need for further study of these materials. In this study, EBSD and SEM-DIC were combined to analyze the relationship between the occurrence of twinning (a secondary deformation mechanism in magnesium) and grain size. It was found that as grain size increased, so did the likelihood that a grain would exhibit at least one twin (Figure 24).

Several data analysis tools, developed by Chen and Daly [15] were incorporated to help automate twin identification for the tested sample. These methods clustered the strain data from DIC, compared the clustered strains to the predicted theoretical strains of all available twin systems, examined the shapes of the clusters using an AlexNet Convolutional Neural Network, and took into account the size evolution of each cluster.

The largest hurdle faced during this study was the computational cost of analyzing the large quantity of data. With 22x22 image tiles, including a total of 184,307,676 DIC data points for each strain component at each strain step, several steps that decreased the accuracy of the analysis were necessary. K-means clustering, used to bin strains into like groups (section 3.4.4 (a)) was chosen for its relatively low computational cost and its ease of use. Other methods, such as adaptive clustering techniques, could improve the accuracy at the cost of time and required computer power. Finally, due to the nature of work with CNN and machine learning, these methods will get better at identifying twins as it is trained with more images of "twinned" and "not twinned" images from different samples under different conditions.

References

1. Agnew, S. R., & Duygulu, Ö. (2005). Plastic anisotropy and the role of non-basal slip in magnesium alloy AZ31B. International Journal of Plasticity, 21(6), 1161-1193. doi:10.1016/j.ijplas.2004.05.018

2. Agnew, S., Yoo, M., & Tomé, C. (2001). Application of texture simulation to understanding mechanical behavior of Mg and solid solution alloys containing Li or Y. *Acta Materialia,49*(20), 4277-4289. doi:10.1016/s1359-6454(01)00297-x

3. Ardeljan, M., Beyerlein, I. J., Mcwilliams, B. A., & Knezevic, M. (2016). Strain rate and temperature sensitive multi-level crystal plasticity model for large plastic deformation behavior: Application to AZ31 magnesium alloy. *International Journal of Plasticity,83*, 90-109. doi:10.1016/j.ijplas.2016.04.005

4. Barnett, M. R. (2007). Twinning and the ductility of magnesium alloys Part I: "Tension" twins. Materials Science and Engineering: A,464(1), 2nd ser. Retrieved May 17, 2017, from http://www.sciencedirect.com/science/article/pii/S0921509306026876

5. Barnett, M. R. (2007). Twinning and the ductility of magnesium alloys: Part II. "Contraction" twins. Materials Science and Engineering: A,464(1), 2nd ser. Retrieved May 17, 2017, from http://www.sciencedirect.com/science/article/pii/S0921509307004297

6. Barnett, M. R., Ghaderi, A., Da Fonseca, J. Q., & Robson, J. D. (2014). Influence of orientation on twin nucleation and growth at low strains in magnesium alloy. Retrieved May 17, 2017, from http://www.sciencedirect.com/science/article/pii/S1359645414005175

7. Barnett, M., Keshavarz, Z., Beer, A., & Atwell, D. (2004). Influence of grain size on the compressive deformation of wrought Mg–3Al–1Zn. Acta Materialia,52(17), 5093-5103. doi:10.1016/j.actamat.2004.07.015

8. Barranger, Y., Doumalin, P., Dupré, J. C., & Germaneau, A. (2012). Strain Measurement by Digital Image Correlation: Influence of Two Types of Speckle Patterns Made from Rigid or Deformable Marks. *Strain*, *48*(5), 357–365. doi: 10.1111/j.1475-1305.2011.00831.x

9. Beyerlein, I. J., Wang, J., Barnett, M. R., & Tome, C. N. (2012). Double twinning mechanisms in magnesium alloys via ... Retrieved May 17, 2017, from http://www.bing.com/cr?IG=2D145559417F4CCDB5F97B89E8BEB107&CID=28BC87 AAD0906C6103678D2FD1006D08&rd=1&h=dnNQc58gY05ULfrTuOaQf3S6AeogpRi DRd3L9Mr31fY&v=1&r=http%3a%2f%2frspa.royalsocietypublishing.org%2fcontent% 2froyprsa%2f468%2f2141%2f1496.full.pdf&p=DevEx,5062.1

10. Beyerlein, I. J., McCabe, R. J., & Tome, C. N. (2011). Effect of microstructure on the nucleation of deformation twins in polycrystalline high-purity magnesium: A multi-scale modeling study. Retrieved May 17, 2017, from http://www.sciencedirect.com/science/article/pii/S0022509611000354

11. Boehlert CJ, Chen Z, Gutiérrez-Urrutia I, et al (2012) In situ analysis of the tensile and tensile-creep deformation mechanisms in rolled AZ31. Acta Mater 60:1889–1904. doi: 10.1016/j.actamat.2011.10.025

12. Boehlert CJ, Cowen CJ, Tamirisakandala S, et al (2006) In situ scanning electron microscopy observations of tensile deformation in a boron-modified Ti-6Al-4V alloy. Scr Mater 55:465–468. doi: 10.1016/j.scriptamat.2006.05.008

13. Carroll J, Abuzaid W, Lambros J, Sehitoglu H (2010) An experimental methodology to relate local strain to microstructural texture. Rev Sci Instrum 81:83703. doi: 10.1063/1.3474902

14. Chapuis, A., & Driver, J. H. (2010). Temperature dependency of slip and twinning in plane strain compressed magnesium single crystals. Acta Materialia, 59(5), 1986-1994. doi:10.1016/j.actamat.2010.11.064

15. Chen, Z., & Daly, S. (2018). Deformation twin identification in magnesium through clustering and computer vision. *Materials Science and Engineering: A,736*, 61-75. doi:10.1016/j.msea.2018.08.083

16. Chen, Z., Lenthe, W., Stinville, J. C., Echlin, M., Pollock, T. M., & Daly, S. (2018). High-Resolution Deformation Mapping Across Large Fields of View Using Scanning Electron Microscopy and Digital Image Correlation. *Experimental Mechanics,58*(9), 1407-1421. doi:10.1007/s11340-018-0419-y

17. Chino, Y., Kimura, K., Hakamada, M., & Mabuchi, M. (2008). Mechanical anisotropy due to twinning in an extruded AZ31 Mg alloy. Materials Science and Engineering: A, 485(1-2), 311-317. doi:10.1016/j.msea.2007.07.076

18. Christian, J., & Mahajan, S. (1995). Deformation twinning. Progress in Materials Science,39(1-2), 1-157. doi:10.1016/0079-6425(94)00007-7

19. Dingley DJ (1969) A simple straining stage for the scanning electron microscope. Micron 1:206–210.

20. Githens, A. (2015). Deformation Mechanisms of Magnesium Alloy WE43 under Monotonic Tensile Loading (Unpublished Master's Thesis). The University of Michigan, Ann Arbor, Michigan.

21. Hoskin GA, Provan JW, Gruzleski JE (1988) The in-situ fatigue testing of a cast aluminum-silicon alloy. Theor Appl Fract Mech 10:27–41.

22. Jain, A., & Agnew, S. (2007). Modeling the temperature dependent effect of twinning on the behavior of magnesium alloy AZ31B sheet. Materials Science and Engineering: A, 462(1-2), 29-36. doi:10.1016/j.msea.2006.03.160

23. Jin H, Lu W, Scheffel S, et al (2007) Full-field characterization of mechanical behavior of polyurethane foams. Int J Solids Struct 44:6930–6944. doi: 10.1016/j.ijsolstr.2007.03.018

24. Kammers AD, Daly S (2013) Digital image correlation under scanning electron microscopy: Methodology and validation. Exp Mech 53:1743–1761. doi: 10.1007/s11340-013-9782-x

25. Kammers AD, Daly S (2013) Self-assembled nanoparticle surface patterning for improved digital image correlation in a scanning electron microscope. Exp Mech 53:1333–1341. doi: 10.1007/s11340-013-9734-5

26. Koike, J., Kobayashi, T., Mukai, T., Watanabe, H., Suzuki, M., Maruyama, K., & Higashi, K. (2003). The activity of non-basal slip systems and dynamic recovery at room temperature in fine-grained AZ31B magnesium alloys. Acta Materialia, 51(7), 2055-2065. doi:10.1016/s1359-6454(03)00005-3

27. Krizhevsky, A., Sutskever, I., & Hinton, G. E. (2017). ImageNet classification with deep convolutional neural networks. *Communications of the ACM*, *60*(6), 84–90. doi: 10.1145/3065386

28. Kumar, M. A., Beyerlein, I. J., & Tome, C. N. (n.d.). Grain size constraints on twin expansion in hexagonal ... Retrieved May 17, 2017, from https://www.bing.com/cr?IG=5789FE7D85D64BB094419D4FCF3B1A6B&CID=3A0E A010102E6DBC3EECAA9511BE6CDA&rd=1&h=vWgJ_HnzQyOfwDJvsOE7nU59nX VxC3QOIPHCVzCuFXU&v=1&r=https%3a%2f%2fwww.researchgate.net%2fprofile% 2fCarlos_Tome%2fpublication%2f309335491_Grain_size_constraints_on_twin_expansi on_in_hexagonal_close_packed_crystals%2flinks%2f5823367708aeebc4f898642e.pdf% 3forigin%3dpublication_list&p=DevEx,5061.1

29. Lenthe, W. C., Stinville, J. C., Echlin, M. P., Chen, Z., Daly, S., & Pollock, T. M. (2018). Advanced detector signal acquisition and electron beam scanning for high resolution SEM imaging. *Ultramicroscopy*, *195*, 93–100. doi: 10.1016/j.ultramic.2018.08.025

30. LePage, W. (n.d.). digitalimagecorrelation.org. Retrieved from https://digitalimagecorrelation.org/#patterning

31. Lewis JP (1995) Fast normalized cross-correlation. Vis Interface 120–123.

32. Lightweight Materials for Cars and Trucks. (n.d.). Retrieved April 12, 2018, from https://www.energy.gov/eere/vehicles/lightweight-materials-cars-and-trucks

33. Luque, A., Ghazisaeidi, M., & Curtin, W. A. (2013). Deformation modes in magnesium (0 0 0 1) and single crystals: Simulations versus experiments. *Modelling and Simulation in*

Materials Science and Engineering,21(4). Retrieved May 29, 2019, from https://iopscience.iop.org/article/10.1088/0965-0393/21/4/045010.

34. Meyers, M., Vöhringer, O., & Lubarda, V. (2001). The onset of twinning in metals: a constitutive description. Acta Materialia,49(19), 4025-4039. doi:10.1016/s1359-6454(01)00300-7

35. Morozumi, S., Kikuchi, M., & Yoshinaga, H. (1976). Electron Microscope Observation in and around {1\bar102} Twins in Magnesium. Transactions of the Japan Institute of Metals,17(3), 158-164. doi:10.2320/matertrans1960.17.158

36. (n.d.). PRISMS Home. Retrieved from http://www.prisms-center.org/#/ctools/software

37. Pilchak AL, Shiveley AR, Shade PA, et al (2012) Using cross-correlation for automated stitching of two-dimensional multi-tile electron backscatter diffraction data. J Microsc 32 248:172–186. doi: 10.1111/j.1365-2818.2012.03661.x

38. Reu, P. (2014). All about Speckles: Aliasing. *Experimental Techniques*, *38*(5), 1–3. doi: 10.1111/ext.12111

39. Reu, P. (2015). All about Speckles: Edge Sharpness. *Experimental Techniques*, *39*(2), 1–2. doi: 10.1111/ext.12139

40. Reu, P. (2014). All about speckles: Speckle Size Measurement. *Experimental Techniques*, *38*(6), 1–2. doi: 10.1111/ext.12110

41. Roberts W, Lehtinen B, Easterling KE (1976) An in situ sem study of void development around inclusions in steel during plastic deformation. Acta Metall 24:745–758. doi: 10.1016/0001-6160(76)90109-7

42. Selvarajou, B., Joshi, S. P., & Benzerga, A. A. (2017). Three dimensional simulations of texture and triaxiality effects on the plasticity of magnesium alloys. Acta Materialia, 127, 54-72. doi:10.1016/j.actamat.2017.01.015

43. Stark, J. P. (1988). Mechanical twinning in crystals. Physical Review B,38(2), 1139-1142. doi:10.1103/physrevb.38.1139

44. Sutton MA, Li N, Garcia D, et al (2007) Scanning electron microscopy for quantitative small and large deformation measurements Part II: Experimental validation for magnifications from 200 to 10,000. Exp Mech 47:789–804. doi: 10.1007/s11340-007-9041-0

45. Sutton MA, Li N, Joy DC, et al (2007) Scanning electron microscopy for quantitative small and large deformation measurements Part I: SEM imaging at magnifications from 200 to 10,000. Exp Mech 47:775–787. doi: 10.1007/s11340-007-9042-z

46. Sutton MA, Orteu JJ, Schreier HW (2009) Image correlation for shape, motion and deformation measurements. Springer, New York, doi. doi: 10.1007/978-0-387-78747-3

47. Sutton MA, Wolters WJ, Peters WH, et al (1983) Determination of displacements using an improved digital correlation method. Image Vis Comput 1:133–139. doi: 10.1016/0262-8856(83)90064-1

48. Vehoff H, Neumann P (1979) In situ sem experiments concerning the mechanism of ductile crack growth. Acta Metall 27:915–920.

49. Wang, J., Beyerlein, I., & Tomé, C. (2010). An atomic and probabilistic perspective on twin nucleation in Mg. *Scripta Materialia*, *63*(7), 741–746. doi: 10.1016/j.scriptamat.2010.01.047

50. Wang, J., Yu, Q., Jiang, Y., & Beyerlein, I. J. (2013, November 12). Twinning-Associated Boundaries in Hexagonal Close-Packed Metals. Retrieved May 17, 2017, from https://link.springer.com/article/10.1007/s11837-013-0803-0

51. Wang, Y., & Huang, J. (2007). The role of twinning and untwinning in yielding behavior in hot-extruded Mg–Al–Zn alloy. Acta Materialia, 55(3), 897-905. doi:10.1016/j.actamat.2006.09.010

52. Zhang, D., Jiang, L., Zheng, B., & Beyerlein, I. J. (2016). Deformation Twinning (Update). Reference Module in Materials Science and Materials Engineering. doi:10.1016/B978-0-12-803581-8.02878-2

53. Zhang, Z., Eakins, D. E., & Dunne, F. P. (2016). On the formation of adiabatic shear bands in textured HCP polycrystals. International Journal of Plasticity, 79, 196-216. doi:10.1016/j.ijplas.2015.12.004